The Meteoritical Society

Meteoritics & Planetary Science 60, Nr 7, 1480–1501 (2025)
doi: 10.1111/maps.14366

Silicate–sulfide interaction within quenched melts of space weathered Ryugu grains

Sylvain LAFORET[1]*, Hugues LEROUX[1], Corentin LE GUILLOU[1], Maya MARINOVA[2], Adrien NÉRI[1], Adrien TEURTRIE[1], Francisco de la PEÑA[1], Damien JACOB[1], Alexandre FADEL[2], and David TROADEC[3]

[1]Université de Lille, CNRS, INRAE, Centrale Lille, UMR 8207-UMET-Unité Matériaux et Transformations, Lille, France
[2]Université de Lille, CNRS, INRAE, Centrale Lille, Université Artois, FR 2638-IMEC-Institut Michel-Eugène Chevreul, Lille, France
[3]Université de Lille, CNRS, Centrale Lille, Junia, Univ. Polytechnique Hauts-de-France, UMR 8520 – IEMN – Institut d'Electronique de Microélectronique et de Nanotechnologie, Lille, France

***Correspondence**
Sylvain Laforet, Université de Lille, CNRS, INRAE, Centrale Lille, UMR 8207-UMET-Unité Matériaux et Transformations, F-59000 Lille, France.
Email: sylv.laforet@orange.fr

(Received 28 June 2024; revision accepted 01 May 2025)

Abstract–The first few microns of the surface of airless bodies are subject to severe changes due to the harsh environment of space, known as space weathering. The Hayabusa2 sample return mission from the asteroid Ryugu provides the first opportunity to study these effects on a carbonaceous and hydrated body. Understanding the structural and chemical changes that occur in the space weathered layers of Ryugu is crucial to correctly interpreting the mechanisms involved in such processes. This study employs transmission electron microscopy to achieve the spatial resolution necessary to analyze the nanoscale heterogeneities in these modified layers. The chemical analyses indicate that features present are likely to represent the spattering of a Ryugu-like material, possibly from a different lithology of the asteroid. However, such material appears to be completely dehydroxylated and depleted in sulfur by approximately 20%. Furthermore, the nanoscale dispersion of vesicles and rounded nanosulfides found in these melt layers helps to estimate the temperatures (>1300°C) and the time scales ($<10^{-8}$ s) involved in their formation. In addition, this study describes and discusses a unique spherical feature not previously observed in Ryugu samples. The 3 µm-sized object shows strong similarities to microchondrules observed in some carbonaceous (CM2) and ordinary chondrites, suggesting a divergent thermal history from that of the melt layers.

INTRODUCTION

The recent Hayabusa2 sample return mission, conducted by the Japanese Aerospace Exploration Agency (JAXA), brought back to the Earth 5.4 g from the surface of the carbonaceous (Cb-type) asteroid (162173) Ryugu. It is thought to have formed in two steps in the main asteroid belt. A first asteroid was first accreted and aqueously altered; then, a subsequent impact caused this asteroid to be fragmented and finally reassembled into its present state (Michel et al., 2020; Watanabe et al., 2019). This disruptive event led to the migration of the asteroid from the main asteroid belt to an inner orbit of the solar system ~5 Myr ago (Okazaki et al., 2023). Ryugu has thus preserved important information about the formation and evolution of planetesimals within the solar system. Ryugu resembles the Ivuna-like carbonaceous chondrites (CI) (Ito et al., 2022; Leroux et al., 2024; Nakamura et al., 2022; Yada et al., 2022; Yokoyama et al., 2022), whose chemical composition is almost identical to that of the bulk solar

system, except for the most volatile elements. The mineralogy of Ryugu samples consists of a highly porous phyllosilicate-rich matrix (>70 vol%), complemented by Fe-Ni-sulfides, magnetites, carbonates, phosphates, and organic matter.

Remote sensing observations of the asteroid in the mid-infrared first indicated the presence of phyllosilicates as an absorption band was detected at 2.7 μm and attributed to the stretching mode of hydroxyl groups (Kitazato et al., 2019, 2021; Sugita et al., 2019). The comparison of this 2.7 μm band intensity between remote sensing and returned samples highlighted major differences as it appears to be half the intensity in remote sensing data than in laboratory measurements. This disparity was interpreted as the result of space weathering processes that modified Ryugu's surface (Matsuoka et al., 2023; Noguchi et al., 2022; Pilorget et al., 2022). In addition, the remote sensing analyses of Ryugu's surfaces suggest that its first 1 m-thick layer formed recently, that is, $<10^6$ years (Sugita et al., 2019), indicating that space weathering occurred in the recent history of Ryugu.

Surface modification of airless bodies is driven by two main effects: solar wind irradiation and high-velocity micrometeorite bombardment (Chapman, 2004; Hapke, 2001; Pieters & Noble, 2016). Solar wind irradiation consists of low-energy ions streaming from the Sun and results in the formation of an amorphous silicate layer typically about a hundred nanometers thick. On the other hand, micrometeorite bombardments describe the impact of interplanetary dust particles at the surface of airless bodies. This process results in cratering, melting, and splashing of the surface material. Space weathering of two anhydrous airless bodies, the Moon and the S-type asteroid Itokawa, has been extensively investigated (Gu et al., 2022; Guo et al., 2022; Huang et al., 2024; Keller & McKay, 1997; Matsumoto et al., 2021; Noble et al., 2005; Noguchi et al., 2011, 2014; Thompson et al., 2014). These studies highlighted the presence of metallic iron nanophases within the amorphous layer that weakens the overall reflectance in the Vis–NIR.

Recovered grains from Ryugu have different types of space weathering features, characterized by amorphous silicate layers. Some of them are interpreted as the result of amorphization by solar wind irradiation and are generally thinner than ~100 nm (Noguchi et al., 2022, 2023). Meanwhile, other surface layers are interpreted as quenched melts produced by micrometeorite impacts and can be as thick as 3 μm (Matsumoto et al., 2023, 2024; Nakato et al., 2023; Noguchi et al., 2022, 2023). In contrast to the anhydrous bodies (the Moon and Itokawa), these melt layers contain abundant and large vesicles, which suggest a degassing process from Ryugu's phyllosilicate-rich matrix (Matsumoto et al., 2023, 2024; Noguchi et al., 2022, 2023). Melt layers also display high densities of round nanosulfides, dispersed within the amorphous silicate. Furthermore, such layers appear to be completely dehydrated and carbon-free (Laforet et al., 2024), confirming the degassing hypothesis.

However, the lack of statistics on these nanoscale space weathering products hinders a full understanding of the processes occurring at the surface of carbonaceous and hydrated airless bodies. Understanding the behavior of the hydrated silicate–sulfide assemblage when exposed to the harsh space environment is key for estimating the thermodynamic conditions that occur during such processes. In this study, we use both scanning and transmission electron microscopy to perform a detailed nanoscale characterization of Ryugu's space weathering products resulting from micrometeorite impacts. This study includes the descriptions of the samples' morphologies and chemical modifications induced by space weathering. Particular attention has been paid to a rigorous quantification of the amount of oxygen in melt layers compared to the underlying phyllosilicates. This work aims to improve the general understanding of space weathering effects on the C-type asteroid Ryugu.

MATERIALS AND METHODS

Selected Grains and Their Handling

JAXA allocated samples to the University of Lille (France). About 80 small grains, typically ~50 μm in diameter, were received from both collection chambers of the spacecraft A (~50 grains) and C (~30 grains). Grains from chamber C were handled at Kyoto University and glued onto an Au plate with epoxy resin (C0105-034). Grains from chamber A are small fragments that have come from a millimetric grain (A0159). They were received loose in a sapphire container (Yada et al., 2022), micromanipulated at the University of Lille, and deposited on a carbon tape for further SEM analyses. A FIB section was also received from JAXA (A0058-C2001-02).

Scanning Electron Microscope

The 80 micrometric grains were studied by scanning electron microscope (SEM), searching for surfaces affected by space weathering, characterized by smooth and/or vesiculated surfaces as described by Noguchi et al. (2022). Before SEM observations, Ryugu grains were coated with an 80 Å chromium layer in order to minimize electron charging effects. Chromium was chosen rather than carbon to avoid confusion with indigenous organic matter. We used a JEOL JSM-7800F LV SEM of the Chevreul Institute (University of Lille).

Images were collected in backscattered and secondary electron modes using a 4 kV accelerating voltage.

Focused Ion Beam preparation

After the identification of regions of interest, five electron transparent foils, about 100–150 nm in thickness, were extracted using focused ion beam (FIB) at the IEMN (University of Lille) with an FEI Strata DB 235. The chosen areas were first protected by depositing a platinum layer. The first part of the extraction process was performed at 15 kV, using a 10 nA probe current. The final part was done at 5 kV and with a 50 pA probe current in order to minimize implantation and amorphization of the sample.

One FIB section was prepared at Kyoto University and received from JAXA (A0058-C2001-02). It was extracted from the surface of grain A0058, after being studied at the SEM at 2 kV and with a 15 pA probe current. Prior to the ion thinning, the target surface was protected with a Pt-C coating. The FIB extraction was performed using a Thermo Fisher Helios FIB–SEM, operating with a 30 kV Ga^+ ion beam. The final thinning process was done using a 12–16 kV Ga^+ ion beams, in order to reach a 150 nm thickness. The damaged layers were removed using a 2 kV Ga^+ ion beam.

Scanning Transmission Electron Microscopy

Scanning Transmission Electron Microscopy (STEM) was performed at the University of Lille on an FEI TITAN Themis 300. The electron source is a Schottky field emission gun. Ryugu thin foils imaging was performed by STEM-HAADF (High Angle Annular Dark Field) using a 300 kV electron beam, an 18 mrad convergence semi-angle, and a 80 pA probe current and collection angles between 50 and 200 mrad. The control of the probe current was performed through the Wien filter type monochromator. Chemical analyses were performed using energy-dispersive X-Ray spectroscopy (STEM-EDXS) using a Thermo-Fisher super-X windowless four quadrant silicon drift detector (SDD). Spectral images were acquired at 300 kV, with a 10 mrad convergence semi-angle and a probe current ranging from 250 to 400 pA. As Ryugu minerals are known to be sensitive to electron beam exposure, short dwell-time per pixel was used (2–8 µs/pixel). The quantification of the STEM-EDXS data was done by applying the absorption correction and by using experimentally determined k-factors for major elements (O, Fe, Mg, Al, S, Ca, and K). The EDXS data sets were processed using the open source software python package HyperSpy (de la Pena et al., 2017). The sulfide size distribution was determined using ImageJ software (Schindelin et al., 2012; Schneider et al., 2012).

STEM-EDXS Oxygen Quantification

Quantifying the oxygen content in the phyllosilicates and the melt layer is key to understand the thermal history of the sample. However, the oxygen signal is highly sensitive to X-ray reabsorption effects. In order to correctly quantify the oxygen in the melt layers, some precautions and approximations were taken. First, in order to limit the bias induced by eventual mass-thickness fluctuations from sample to sample, our comparisons only focus on hyperspectral maps covering both melt layers and matrix to ensure that they have the same thickness. Second, we assume that C-rich matter represents less than 5 atom% of the Ryugu matrix, and that only a small proportion of it is associated with O (O/C ratio = 0.04–0.12, Yabuta et al., 2023) representing overall only a few tenths of a percent of the total O content. Concerning the melt layers, it has been shown that they are depleted in carbon (Laforet et al., 2024). In both cases, we neglect the contribution of O from Ryugu organics. Third, we assume that no interlayer water is present in smectites and consider that only hydroxyl groups are present in the phyllosilicates (saponite–serpentine mixture). Indeed, preliminary analyses of saponite described a lack of water in their interlayer space (Nakamura et al., 2022; Noguchi et al., 2022; Yokoyama et al., 2022). Furthermore, under high vacuum conditions in the TEM (10^{-5} Pa), the interlayer water molecules are desorbed. Without considering the hydrogen, as it cannot be measured using EDXS, the phyllosilicates' oxygen content should be 64 atom% in serpentine and 63 atom% in saponite.

Taking this O content in the matrix as a reference, we relatively determined its mass thickness so that the absorption correction provides the correct oxygen quantification. Afterward, the signal intensities from both the matrix and melt layer were normalized to the pixel and compared. The mass thickness of the silicate material of the melt layer was obtained by multiplying the ratio of these two intensities by the mass thickness of the matrix.

In order to only select the signal from silicates, sulfides and other Fe-bearing minerals are masked based on the Fe/Mg and the S/Mg EDXS ratios. Pixels for which either of these two ratios exceed 0.7 are masked and thus are not considered for quantitative analyses.

RESULTS

Morphology of Ryugu Grains

SEM observations of Ryugu grains allow the identification of surfaces affected by space weathering.

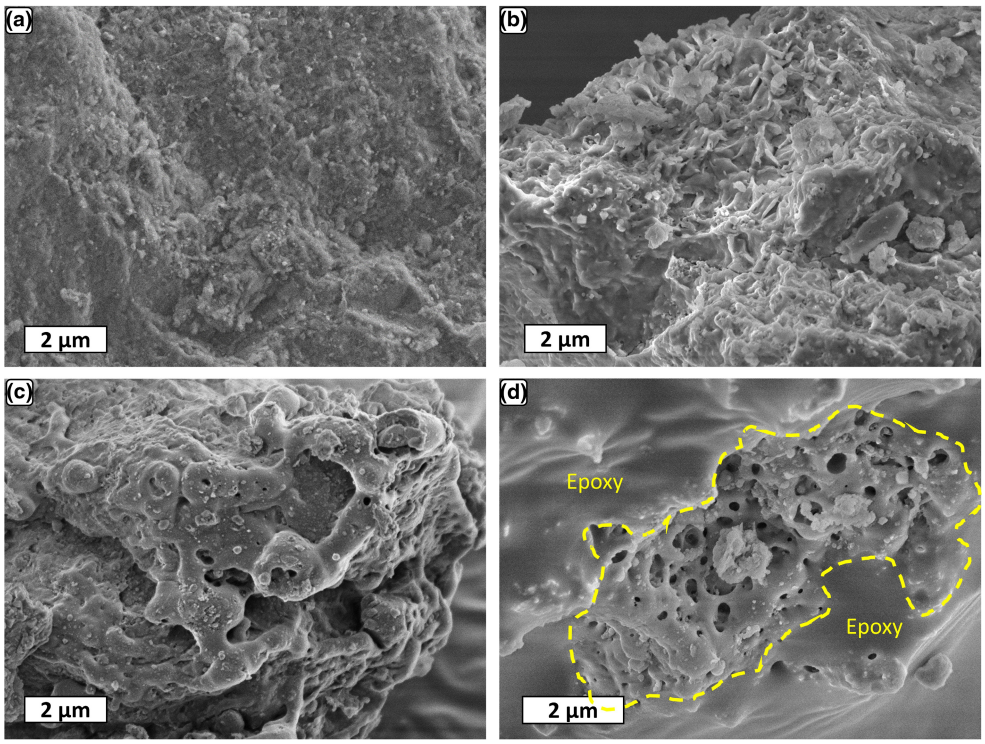

FIGURE 1. SEM-secondary electron images of Ryugu grains showing gradual space weathering effects. (a) Fibrous surface of an unweathered grain; (b) smooth surface that may be the result of solar wind irradiation; (c) and (d) vesiculated surfaces (melt layers) of space weathered grains (samples C0105-034-006/C0105-034-010b/A0159_002_008/C0105-034-001d). (Color figure can be viewed at wileyonlinelibrary.com)

Commonly, the surface aspect of the grains is fibrous due to the dominant phyllosilicate-rich mineralogy of Ryugu, which represents more than 70 vol% of the mineralogy (Figure 1a). Among the ~80 grains analyzed in this study, six of them show a modified aspect of their surface, corresponding to ~7.5% of the observations. This ratio is consistent with the range of 6%–7% observed in the Hayabusa2 collection (Noguchi et al., 2022, 2023). It includes the occurrence of a smooth and continuous layer that coats the grain without any vesicles. These smooth layers sometimes reveal the topography of the underlying matrix (Figure 1b). Some others present the occurrence of rare and tiny vesicles trapped within the silicate (Figure 1c). A few surfaces show further development of vesicles, which can reach a few hundreds of nanometers in diameter, forming a highly spongy surface (Figure 1d). When identified at the surface of a grain, these vesiculated textures rarely cover more than a few tens of μm^2.

Microtexture of Melt Layers

FIB sections were extracted from vesiculated surfaces. TEM and Scanning-TEM (STEM) characterization reveal that the layer thicknesses range from a few hundred nanometers (Figure 2c,d) to a few micrometers (Figure 2a,b,g,h). Such layers consist of a silicate glass matrix containing numerous round nanosulfides and vesicles, as observed by Noguchi et al. (2022). The glassy nature of the silicate is confirmed by the absence of diffraction contrast. An iron oxide has also been observed in one melt layer (Figure 2d). The size of both vesicles and nanosulfides ranges from a few nanometers to several hundred nanometers. The interfaces between the melt layers and the fresh underlying matrix are generally well defined. In most cases, these interfaces do not show the presence of vesicles (Figure 2a–f). However, in some cases, large vesicles can be present (Figure 2g,h).

One of the grains shows the presence of glass layers covering a large part of its surface, including when the faces are opposite (Figure 3). The ~10 µm grain exhibits a discontinuous layer of silicate glass containing rounded nanosulfides and vesicles. The shape of the grain is quite irregular, and the glass layer covers both roughness and cavities. These features are typically 200–500 nm thick.

Bulk Silicate Chemical Comparison Between Melt Layers and Phyllosilicate-Rich Matrix

Major elements present in the silicate material (Mg, Si and Fe) do not show significant concentration variations between melt layers and the phyllosilicate

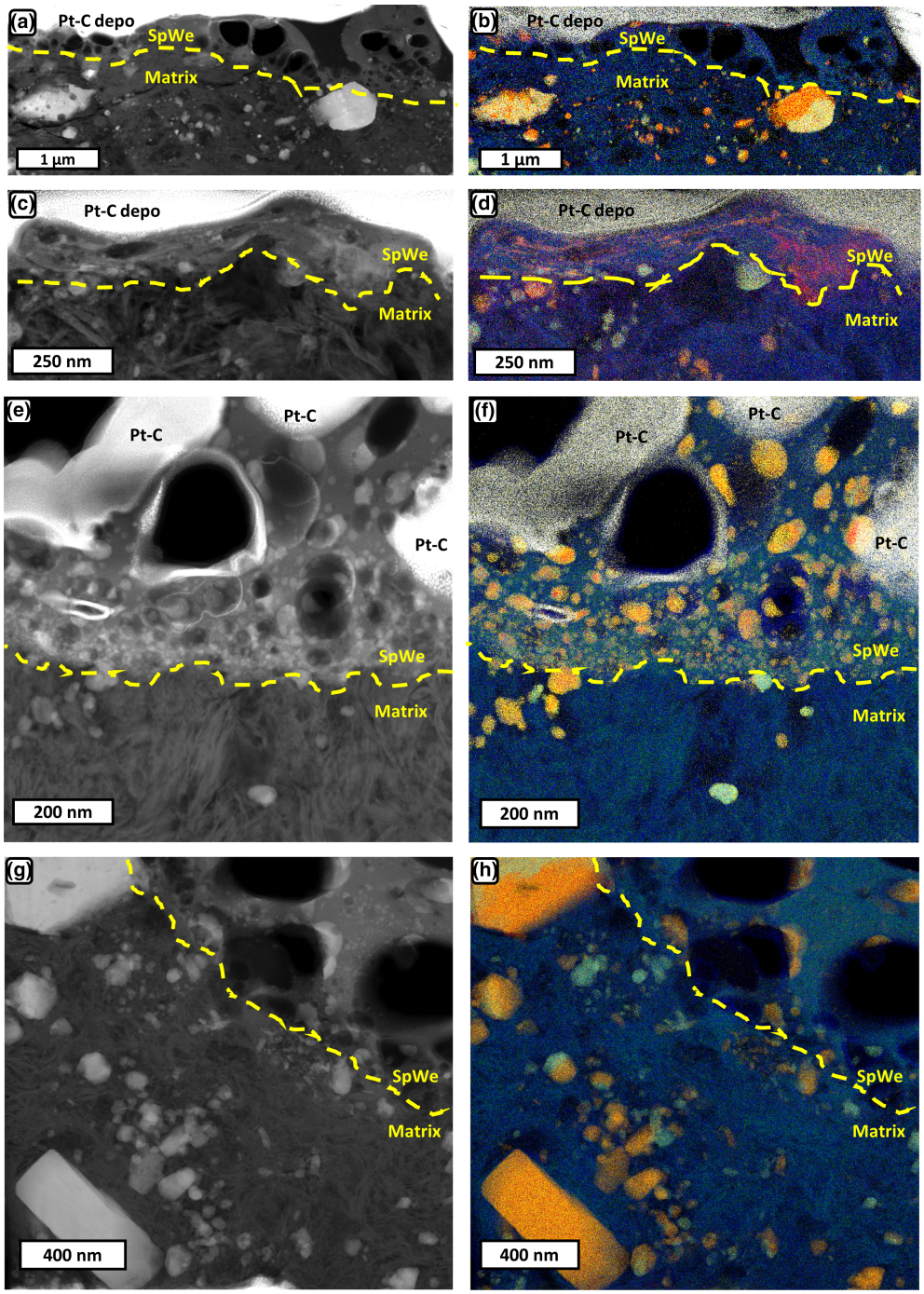

FIGURE 2. STEM-HAADF images (left column) and STEM-EDXS color maps (right column; Si = Blue, Mg = Green, Fe = Red, S=Yellow, Ni = Cyan). In the X-ray maps, the silicates appear as blue/green, pentlandites in cyan, pyrrhotites in orange, and magnetites in red. Yellow dashed lines separate the unweathered phyllosilicate-rich matrix from the melt layer (SpWe). (a, b) Melt layer contains large vesicles and a few nanosulfides. Note the variable thickness of the melt layer that ranges from a few tens of nm to ~1 µm (sample C0105-034-001d02). (c, d) 200 nm thick melt layer containing only a few vesicles. The nanosulfides are small, typically ~20 nm, and display an elongated shape, parallel to the grain surface (sample C0105-034-016b01). (e, f) Thick melt layer containing a high density of nanosulfides at the interface between the melt layer and the underlying matrix. Note that this interface is sharp (C0105-034-014a01). (g, h) Melt layer showing large vesicles located close to the interface (sample A0058-C2001-02). (Color figure can be viewed at wileyonlinelibrary.com)

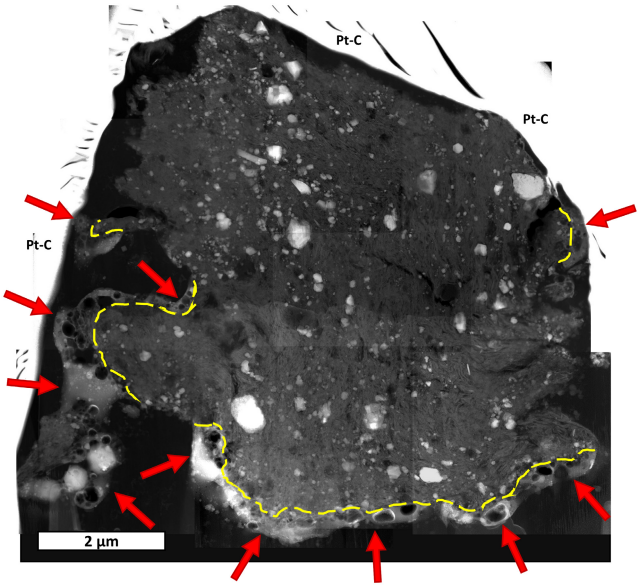

FIGURE 3. Mosaic of STEM-HAADF images of a cross section C0105-034-001d01 extracted from grain C0105-034-001d. This sample shows space weathering features that cover the major part of its surface (red arrows). The interface with the unweathered matrix is represented by the yellow dashed line. (Color figure can be viewed at wileyonlinelibrary.com)

pristine material. However, melt layers seem to be slightly Fe-enriched and Si-depleted (cf. Fe/(Fe + Mg) and (Mg + Fe)/Si ratios in Table 1; Figure 4).

Regarding minor elements, Al concentration ranges from 1 to 1.6 atom%, with no clear distinctionbetween melt layers and fresh phyllosilicate-rich matrix. On the other hand, strong Na concentration variations occur. Sodium concentrations are 2× higher in the matrix compared to the melt layer in grain *C0105-034-001d02*, but they are lower in another (by 3.2 atom% in *C0105-034-01701*). Other minor elements present in the silicate matrix (Ca, Cr, K, Ni and S) count for only a few tenths of a percent of the total composition.

Our STEM-EDXS oxygen quantification in the silicate material of melt layers relies on the approximation that the underlying phyllosilicate mixture is fully hydroxylated and that it does not contain interlayer water. Therefore, we can determine its oxygen content by first estimating the proportion of serpentine and saponite within the phyllosilicate-rich matrix, which can be obtained from the cations/Si ratio (here, cations are Mg and Fe). In pure serpentine, the cations/Si ratio is 1.5, whereas it is ~0.75 in saponite. The results presented in Table 1 show that this ratio is about 1 in the Ryugu matrix (Table 1), leading us to deduce that the phyllosilicate matrix contains approximately one-third of serpentine and two-thirds of saponite. It appears that this ratio is not affected by the absorption correction procedure as Si, Mg, Fe, and Al are not highly sensitive to reabsorption effects. Thus, the oxygen content in the matrix should theoretically be 63.3 atom% assuming that there is no interlayer water in saponite (Nakamura et al., 2022; Noguchi et al., 2022; Yokoyama et al., 2022). Results in the melt layer show a significant loss of oxygen from the matrix to melt layers, from 63.3 to 58.3 atom% on average.

Nanosulfides Size Distribution and Compositions

We analyzed the size and composition of sulfides based on HAADF images and STEM-EDXS color maps (Figures 2 and 5). While the matrix contains a large amount of euhedral sulfides, whose sizes range from 15 to 150 nm, melt layers have a high density of smaller and rounded sulfides whose diameter rarely exceeds 75 nm. In some cases, a high concentration of nanosulfides is present near the interface with the unmodified material (Figure 2e,f). In other cases, sulfides from the melt layers sometimes adopt elongated shapes, with an elongation parallel to the interface with the underlying phyllosilicates (Figure 2c,d). Figure 5 shows the nanosulfide size distributions from both matrix and melt layer. The two distributions both show an asymmetrical shape. However, they are clearly distinguishable, with median values at 14 nm for melt layers' and 46 nm in the matrix. Furthermore, their respective standard deviations are also different, with a smaller deviation in the melt layers compared to the matrix.

When looking at the sulfide size distribution as a function of their distance to the interface between the melt layer and the phyllosilicate-rich matrix, it appears that a size gradient occurs, with the smallest sulfides being closest to the interface (Figure 6). Between 0 and 100 nm from the interface, they range in diameter from 10 to 20 nm, while they can reach 40–100 nm at 300 nm and beyond (Figure 6).

In addition to rare sphalerite (Fe-Zn-S), sulfides in the phyllosilicate matrix have two distinct populations, for example, pyrrhotite and pentlandite (Figure 7). Instead, sulfides in the melt layer have an intermediate composition whose value is at the average of the matrix sulfides. The composition lies between Ni/(Ni + Fe) = 0 and Ni/(Ni + Fe) = 0.15 (Figure 7).

Averaged sulfide composition of the matrix and the melt layers exhibits a Ni/(Ni + Fe) ratio of 21% and 17%, respectively. A S depletion is observed in the melt (S/(Fe + Ni) =0.95), compared to the matrix (S/(Fe + Ni) =1.20).

Within the melt layer, the Ni content of the largest sulfides (~150 to 200 nm in diameter) seems heterogeneous (Figure 8b, *sulfide 1*). In some of them, it appears that the Ni/(Fe + Ni) ratio histogram only

TABLE 1. Average chemical comparison (in atom%) of the silicate material from melt layers and the unweathered phyllosilicate-rich matrix based on STEM-EDS hyperspectral maps shown in Figure 1.

	Element													
Sample	Mass thickness ($g\,cm^{-2}$)	O	Na	Mg	Al	Si	S	K	Ca	Cr	Fe	Ni	Fe/Fe + Mg	Mg + Fe/ Si
A0058-C2001-02 Matrix	5.9×10^{-5}	63.3	n.d.	13	1.3	17.3	0.6	n.d.	0.1	0.2	3.7	0.2	0.22	0.97
A0058-C2001-02 Melt	9.9×10^{-5}	58.9	1.7	15.7	1.4	15.4	1	n.d.	0.2	0.1	5.4	0.1	0.25	1.37
C0105-034-01d02 Matrix	5.3×10^{-5}	63.3	4	12.6	1	13.7	1.7	0.1	0.1	0.1	2.8	0.3	0.18	1.12
C0105-034-01d02 Melt	5.4×10^{-5}	54.7	8	14	1.2	16.3	1.4	0.1	n.d.	0.2	3.6	0.3	0.2	1.08
C0105-034-16b01 Matrix	7.4×10^{-5}	63.3	3.2	13.3	1.3	15.5	0.3	0.1	n.d.	0.2	2.7	n.d.	0.17	1.03
C0105-034-16b01 Melt	8.8×10^{-5}	59.6	2.4	15.3	1.4	15.2	1	n.d.	n.d.	1.1	3.7	0.2	0.19	1.25
C0105-034-14a01 Matrix	5.3×10^{-5}	63.3	0.5	15.2	1.2	17	0.1	n.d.	n.d.	0.1	2.2	n.d.	0.13	1.02
C0105-034-14a01 Melt	4.8×10^{-5}	56.9	1	16.1	1.4	18.6	1.2	n.d.	0.1	0.1	4.5	n.d.	0.22	1.11
C0105-034-1701 Matrix	3.5×10^{-5}	63.3	3.2	13.5	1.1	14.2	1.3	0.1	0.1	0.3	2.7	0.1	0.17	1.14
C0105-034-1701 Melt	5.8×10^{-5}	61.3	n.d.	18.2	1.6	15.7	0.1	n.d.	n.d.	0.2	2.6	n.d.	0.12	1.32
Mean matrix	5.5×10^{-5}	63.3	2.7	13.5	1.2	15.5	0.8	n.d.	0.1	0.2	2.8	0.2	0.17	1.05
Mean melt	7.0×10^{-5}	58.3	3.3	15.9	1.4	16.2	0.9	n.d.	0.2	0.3	4.0	0.2	0.20	1.22

Note: The mass thickness of the matrix was set in order to obtain a 63.3 atom% of O after absorption correction, which corresponds to the O concentration in a 33%–67% serpentine/saponite mix (assuming that there is no interlayer water in the saponite).
Abbreviation: n.d., not detected.

describes one population. In others, this Ni/(Fe + Ni) ratio fluctuates from 0 to 0.4 (Figure 8b,c, *sulfide 2*). When averaged, these ratios are 0.12 and 0.16 (Figure 8c), which are lower than what has been observed on larger scale analyses (~0.17).

Sulfur distribution in sulfides from melt layers is homogeneous and centered around S/(Fe + Ni) = 0.95 (Figure 7). In addition, it appears that vesicles are also present within the sulfides (Figure 8a).

Silicate Droplet

We identified by SEM a singular ~3 μm large spherical silicate droplet, occurring on a grain surface (Figure 9a). The droplet surface is extremely smooth. The top of the droplet is covered by phyllosilicates. The FIB section reveals that it is made of an amorphous silicate with diametrically opposed Fe-rich metal and sulfide lobes at its surface (Figure 9b,c). Unlike other melt layers presented in this study, the droplet does not contain vesicles, and only a few small rounded Fe-rich inclusions remain.

The droplet silicate composition is homogeneous and shows chemical differences compared to melt layers (Table 1). The Fe/(Mg + Fe) is ~0.12 in the droplet, whereas it is usually about 0.17 in other melt layers. In addition, the (Mg + Fe)/Si ratio of the droplet, estimated at 1.32, is high compared to other silicate glasses (Table 1).

The oval-shaped Fe-rich regions are stretched parallel to the surface of the silicate droplet, which ends in an acute angle. They are made of Fe-sulfide and metallic Fe-Ni domains with an Ni/(Ni + Fe) = 0.2 (Figure 10). These areas are typically 10 nanometers wide and form an intertwined network of interconnected domains. The sulfide is more abundant than the Fe-Ni alloy as the averaged composition of both left and right Fe-rich lobes (Figure 9b,c), respectively, $Fe_{0.60}Ni_{0.13}S_{0.27}$ and $Fe_{0.59}Ni_{0.08}S_{0.33}$, is closer to the Fe-sulfide pole (Figure 10c). This leads to a volume proportion of 55% Fe sulfides and 45% Fe-Ni alloy in the left lobe, and a 64%–36% in the right one. The lobe–silicate interface consists of a sulfide layer, while the outer part of the lobe is covered by a continuous metallic Fe-Ni layer about ~10 nm thick (Figure 10b).

Rare Fe-rich inclusions (~10) occur inside the droplet ranging from few tens of nm to 80 nm

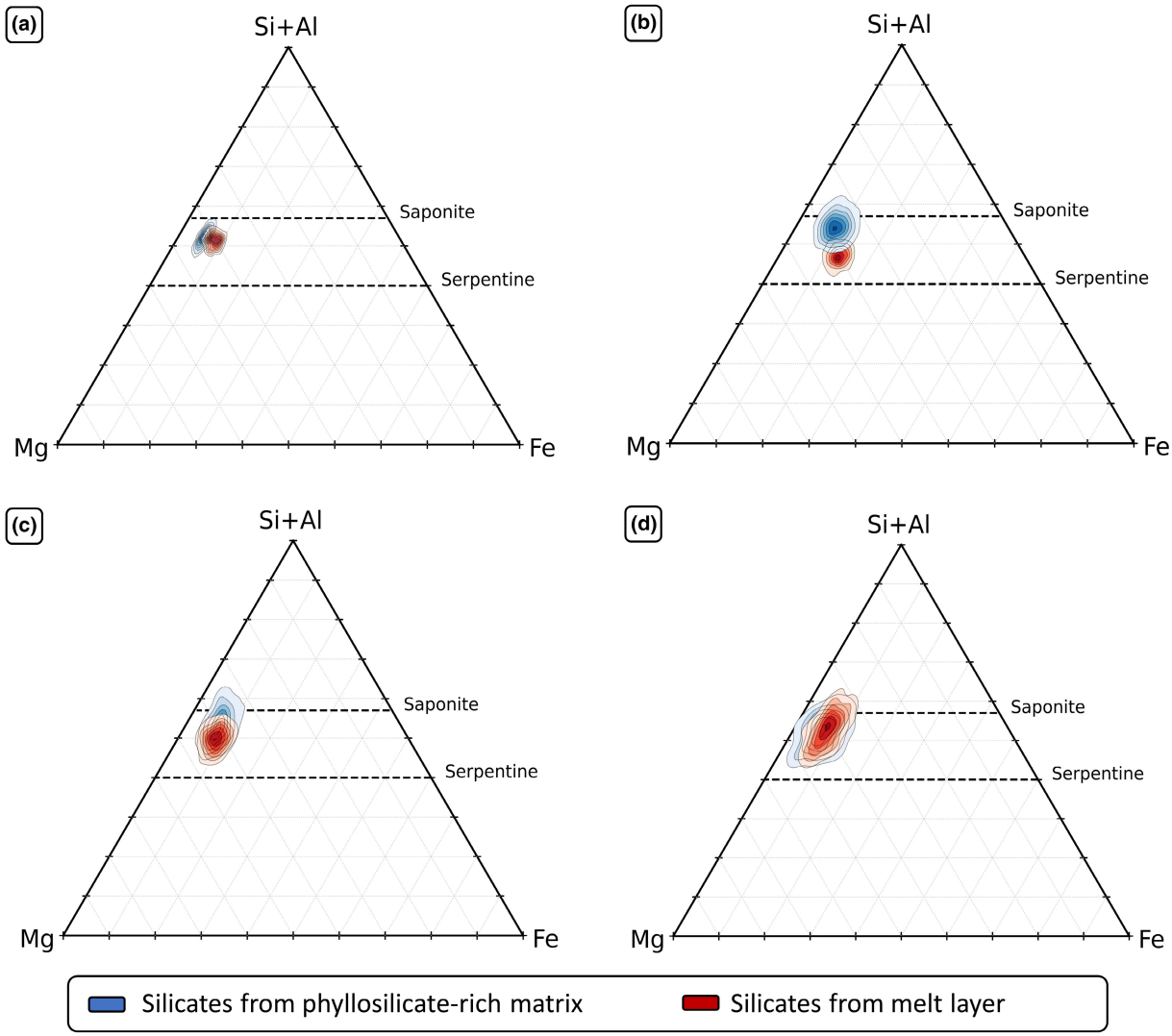

FIGURE 4. (Si + Al)-Mg-Fe ternary diagrams comparing the silicate melt layer compositions with the underlying fresh phyllosilicate-rich matrix. For each data set, the sulfide contributions are corrected as follows: $Fe_c = Fe–S$. The contour plots come from pixel per pixel analyses and describe a density of points. The pixel sizes range from 15×15 to $18 \times 18\ nm^2$ depending on the data. (a) C0105-034-014a01, (b) A0058-C2001-02, (c) C0105-034-016b01, (d) C0105-034-001d02. (Color figure can be viewed at wileyonlinelibrary.com)

(Figure 11a,b). The inclusions show a phase segregation, forming a core–shell structure. A principal component analysis performed on the STEM-EDXS data enabled the two different compositions to be distinguished. The shells have an Fe-sulfide composition and the core interiors a metallic Fe composition (Figure S1). In addition, it appears that the shells contain tiny particles that display a high contrast in the HAADF image (Figure 11a). Their size does not exceed few nanometers in diameter, which renders their compositional analysis difficult. However, the contrast they display suggests that the lumps are probably small, metallic Fe inclusions.

A singular feature is observed at the surface of the droplet (Figure 12). Locally, the droplet is covered by a layer made of two distinct phases. One corresponds to a vesiculated iron oxide, and the other is almost a pure stoichiometric Ni sulfide. These layers range from 50 to 150 nm in thickness and occur in continuity with one another. The iron oxide layer displays a vesiculated aspect. It is located on top of a vesiculated area of the silicate glass, which also appears to be placed on the spherical droplet. A few vesicles are trapped inside this silicate material, whereas none are observed in the large droplet. At the location where this vesiculated silicate glass is located, the perfect sphericity of the ball is locally disrupted.

Chemical analysis of the vesiculated silicate area (Table 2) allows the identification of an enrichment in Na

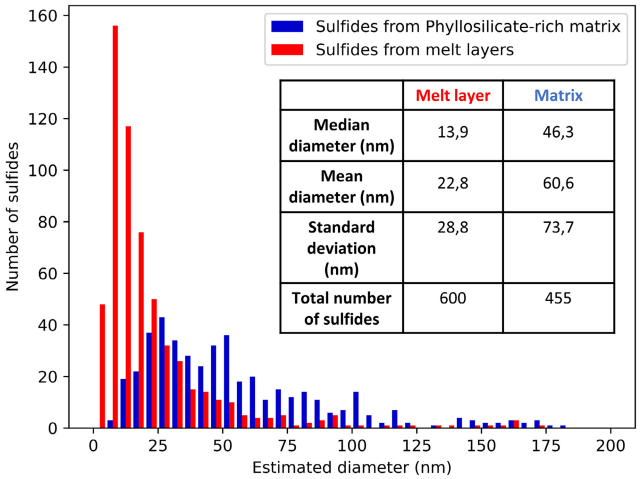

	Melt layer	Matrix
Median diameter (nm)	13,9	46,3
Mean diameter (nm)	22,8	60,6
Standard deviation (nm)	28,8	73,7
Total number of sulfides	600	455

FIGURE 5. Sulfide size distribution comparison between melt layers and unweathered phyllosilicate-rich matrix. Sulfides were isolated by hand using ImageJ software as automated methods were unable to differentiate overlapping sulfides, thus inducing a bias. (Color figure can be viewed at wileyonlinelibrary.com)

compared to the rest of the silicate droplet. Additionally, the Fe/(Fe + Mg) ratio of 0.17 in the vesiculated silicate differs from the one measured in the silicate droplet (0.12). Overall, the (Mg + Fe)/Si ratio is identical between the two silicates.

DISCUSSION

Chemical Evolution, Dehydroxylation, and Sulfur-Loss

This study of Ryugu glassy layers chemistry opens the door to interpreting their origin and formation mechanisms on the surface of carbonaceous asteroids. The glassy silicate, vesicles, and rounded nanosulfides observed in micrometer-sized space weathered layers of Ryugu (Figure 2) display similar microstructural textures as in previous studies (Matsumoto et al., 2023, 2024; Noguchi et al., 2022, 2023). Such structures have been attributed to high-velocity impacts of micrometeorites, forming so-called *melt layers* (Noguchi et al., 2022, 2023). High-velocity impacts experiments and heating studies of Murchison (CM2) and micrometeorites performed by Nozaki et al. (2006) and Noguchi et al. (2007) interpreted the formation of silicate melts and vesicles to occur above 1000°C. In addition, the thermochemical description of the Fe-Ni-S ternary system first proposed by Hsieh et al. (1982) and further described by Waldner and Pelton (2004) indicates that both pyrrhotite and pentlandite melt to form a single liquid composition above 1200°C. Concerning the phyllosilicates initially present in the Ryugu matrix, their dehydroxylation occurs around 600°C (Yokoyama et al., 2022). It results in a silicate with a basaltic composition, which is known to melt below 1300°C (Chen et al., 2017; Shaw, 1969). These observations suggest that the molten material of Ryugu experienced temperatures above 1200–1300°C to melt and emulsify both silicate and sulfides.

Previous works highlighted a loss of volatiles in Ryugu melt layers such as oxygen and carbon (Laforet et al., 2024; Matsumoto et al., 2024; Noguchi et al., 2022, 2023). Our goal here has been to quantitatively determine the chemical differences between the melt layers and the underlying matrix. Our results underline notable changes when it comes to most volatile elements. In the silicate material, the oxygen content drops from 63.3 atom% in the matrix to 58.3 atom% on average in melt layers with a 2.2% standard deviation. As a comparison, a silicate glass resulting from the full dehydroxylation of a 67%–33% saponite–serpentine mixture should theoretically contain 58.2 atom% of oxygen. This quantification of oxygen in melt layers indicates that they are partially, if not completely, dehydroxylated.

The sulfides also underwent chemical changes: Their composition is homogenized. They are present as pyrrhotite and pentlandite in the matrix and evolve to an intermediate composition in the melt layers (Figure 6). The sulfur content appears to be significantly lower in melt layers than in the unweathered matrix, similar to what has been observed in other melt layers from Ryugu, Itokawa, the Moon, as well as in space weathering simulating experiments (Chaves & Thompson, 2022; Loeffler et al., 2008; Matsumoto et al., 2020, 2021, 2023). We observed that the average S/(Fe + Ni) ratio drops from 1.20 in matrix sulfides to 0.95 in melt layer sulfides (~20% loss), attesting to its volatility (Figure 7). Chaves and Thompson (2022) determined 30% of sulfur loss in Itokawa sulfides, suggesting more energetical space weathering events. In Ryugu, the Fe-rich lobes of the silicate droplet show stronger sulfur losses as they display S/(Fe + Ni) atom ratios of 0.37 (left lobe) and 0.49 (right lobe), possibly due to a longer duration of the high-temperature phase compared to other melt layers. Furthermore, the smaller size of the left lobe of the droplet compared to the right one likely led to faster loss of sulfur as their respective compositions are $Fe_{0.59}Ni_{0.08}S_{0.33}$ and $Fe_{0.60}Ni_{0.13}S_{0.27}$. This result suggests that the sulfur loss is enhanced when the surface of the interface with the vacuum is large compared to the volume of the lobe. In the context of silicate–sulfide interaction during brief high-temperature events such as impacts, several studies highlighted similar sulfur losses from the sulfides. This effect is particularly marked in the cometary samples from the Stardust mission. These cometary grains were flash heated at temperatures above 1500°C when undergoing deceleration in the aerogel, and cooled by heat dissipation within a few microseconds.

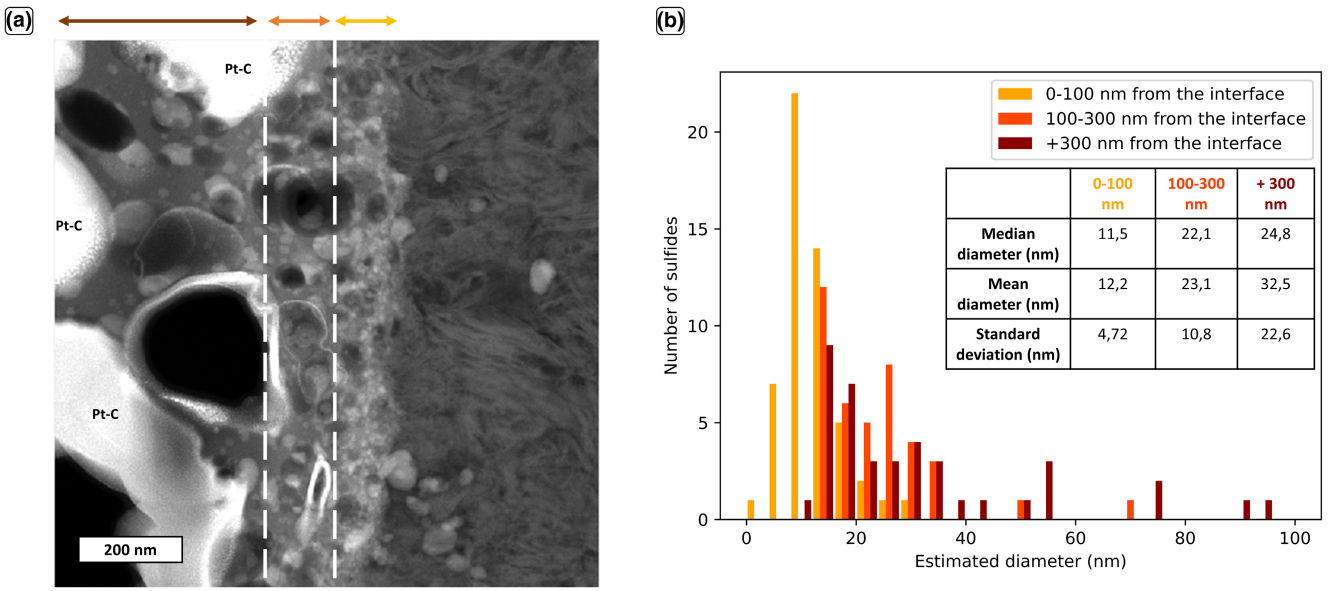

	0-100 nm	100-300 nm	+ 300 nm
Median diameter (nm)	11,5	22,1	24,8
Mean diameter (nm)	12,2	23,1	32,5
Standard deviation (nm)	4,72	10,8	22,6

FIGURE 6. (a) STEM-HAADF image of sample C0105-034-014a01. Three regions with distinct distances from the interface (yellow dashed line) are identified in order to measure (b) their sulfide size distributions. Sulfides were isolated by hand using ImageJ software. (Color figure can be viewed at wileyonlinelibrary.com)

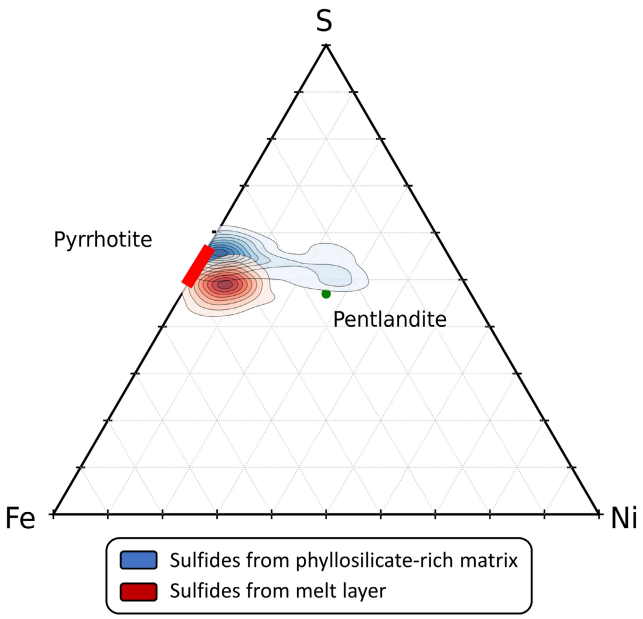

FIGURE 7. Fe-Ni-S ternary diagram (in atom%) illustrating the differences in sulfide compositions between melt layer and the underlying phyllosilicate-rich matrix (in blue) (sample A0058-C2001-02). When dealing with small size objects (few nanometers), the X-ray signal from different phases can overlap (pixel size = 20 nm). To avoid this phenomenon, the contribution of the Fe carried by the silicates has been corrected using the Fe/(Fe + Mg) ratio in Table 1: $Fe_c = Fe - 0.22*Mg$ for the phyllosilicates, $Fe_c = Fe–0.25*Mg$ for the melt layer. (Color figure can be viewed at wileyonlinelibrary.com)

This led to silicate–sulfide emulsions and core–shell structures within the Fe-rich nanophases (Leroux, 2012; Leroux et al., 2008). Other examples of flash heating are the fusion crusts of chondrites and the cosmic spherules (melted micrometeorites) formed during atmospheric entry. They reached temperatures ranging between 1000 and 1700°C during 1 or 2 s (Genge, 2017; Love & Brownlee, 1991; Panerai et al., 2021; Suttle, Genge, Folco, et al., 2019; Suttle, Genge, Salge, et al., 2019; Taylor et al., 2011). For example, the CM2 Winchcombe chondrite, which likely originates from a rubble pile asteroid (King et al., 2022; Suttle et al., 2022), shows S/(Fe + Ni) atom% ratios of 0.55 within the fusion crust, whereas the pristine sulfides have a 1.05 ratio, interpreted as the result of volatilization and loss of sulfur during the high-temperature event (Genge et al., 2023; Genge & Grady, 1999). The fusion crusts of micrometeorites frequently show pumice structures, sometimes containing Fe-rich lobes (Taylor et al., 2011). Within these lobes, Taylor et al. (2011) underlined the evaporation of sulfur and the formation of metallic Fe-Ni domains intermixed with the sulfide, similar to what is observed in the lobes of the silicate droplet of the present study (Figure 10).

Another extreme case of a high-temperature event is embodied by the silicate droplet, as it adopts a perfectly spherical shape, no vesicles, and a clear segregation between the silicate and the Fe-rich phases (Figure 9). Its texture clearly differs from the other melt layers, which contain

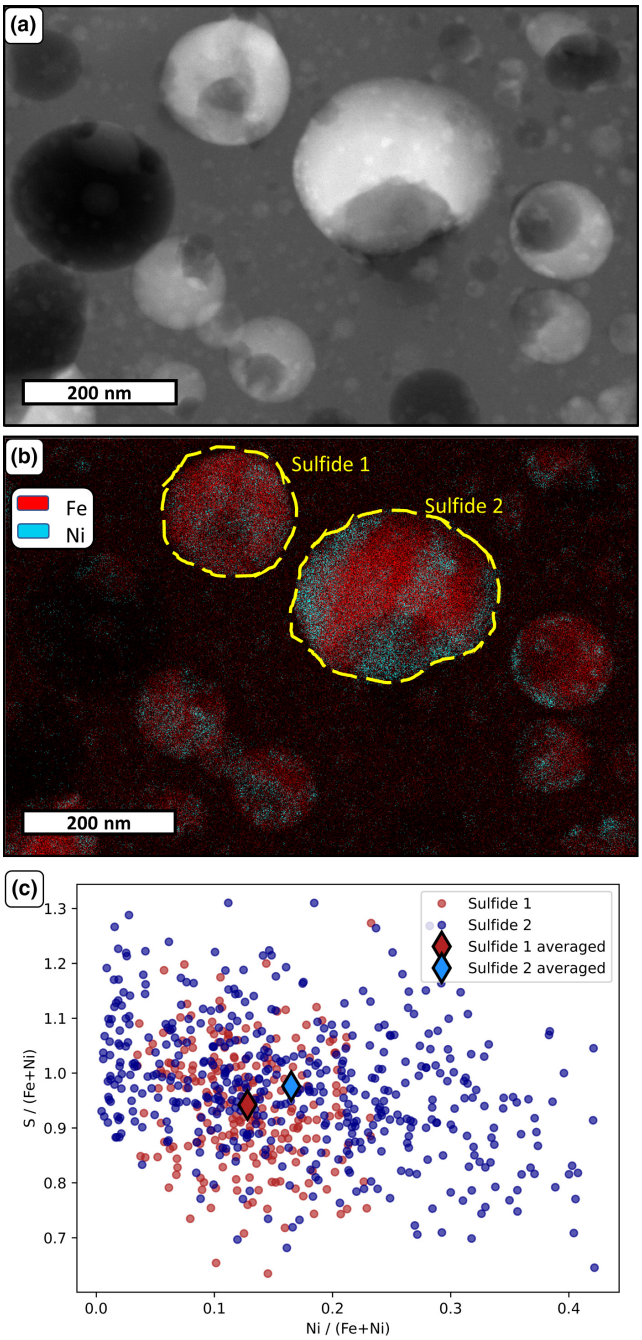

FIGURE 8. Variation in composition of large sulfides (>150 nm) from melt layers: (a) STEM HAADF image of a melt layer containing numerous rounded nanosulfides (sample A0058-C2001-02). The tiny bright spots in the large sulfide droplets are likely due to the presence of small sulfides above or below the bigger ones, that is, in the volume of the FIB lamellae. (b) STEM-EDXS color map based on the signal intensity of the different elements. (c) S/(Fe + Ni) versus Ni/(Fe + Ni) histograms illustrating that sulfides 1 and 2 have heterogeneities in Ni and S in the melt layer (in atom%). The contribution of Fe carried by the silicates has been corrected using the Fe/(Fe + Mg) ratio in Table 1: $Fe_c = Fe–0.25 \times Mg$. Each pixel has a $9 \times 9\ nm^2$ size. (Color figure can be viewed at wileyonlinelibrary.com)

abundant vesicles and nanosulfide inclusions (Figure 2). Furthermore, it shows more advanced chemical modifications that tend to share structural similarities with another intriguing structure found in Ryugu by Matsumoto et al. (2024). Located on top of a Ryugu grain, the latter describes the presence of an amorphous silicate layer lacking vesicles, containing Fe-rich core-shell inclusions, and capped by a micrometer-sized Fe-rich lobe. In the present study, the sulfur of the Fe-rich lobes has been further mobilized, leading to the formation of a metallic alloy (Figure 13) similar to the Fe-rich lobes of Matsumoto et al. (2024). Here, this loss of sulfur is accompanied by a loss of nickel as the overall composition of the Fe-rich lobes shows an Ni/(Ni + Fe) atom% ratio of 0.14 where it is about 0.17 in melt layer sulfides. Previous studies focused on matrix sulfides quantified the proportion of Ni-rich sulfides at ~40–50 vol%, which leads to Ni/(Ni + Fe) atom% ratios of 0.2–0.25 (Leroux et al., 2024; Noguchi et al., 2023). This difference suggests that nickel was also mobilized during the high-temperature event. Therefore, the silicate droplet has likely undergone a longer high-temperature period that led to the further loss of S and Ni. Furthermore, Chaves and Thompson (2022) described similar losses of Ni in space weathered pentlandites from Itokawa (10% loss of Ni). In Ryugu, an Ni depletion has been described at the surface of a modified pentlandite (Matsumoto et al., 2022). These observations underline the possibility that Ni and S may be lost together during the space weathering event. As discussed by Chaves and Thompson (2022), the fact that Ni-S has shorter and stronger bonds than Fe-S makes possible the evaporation of these elements as a molecule rather than as individual atoms. Therefore, the singular Ni-S layer observed at the surface of the droplet (Figure 12) possibly results from a loss of gaseous Ni-S during the high-temperature event that later recondensed.

The occurrence of vesicles in melt layers attests that degassing took place during the high-temperature event. This degassing may have different origins: (i) dehydroxylation of phyllosilicates, (ii) loss of sulfur from the sulfides, likely in the form of H_2S gas (Chaves & Thompson, 2022), and (iii) the decomposition of organic matter leading to carbon oxide gases. Such decomposition comes along with the reduction of iron (Laforet et al., 2024; Noguchi et al., 2022). The vesicles resulting from degassing are found in every Ryugu melt layer (Figure 2). Their sizes, ranging from a few nanometers to a few hundred nanometers, indicate that they had different dynamic histories that led to various degrees of coalescence.

Cooling Time Scales of the Molten Materials

Our study showed that there are two configurations of molten materials: molten layers (Figure 2) and molten spherules (Figure 9). In this section, we will estimate the

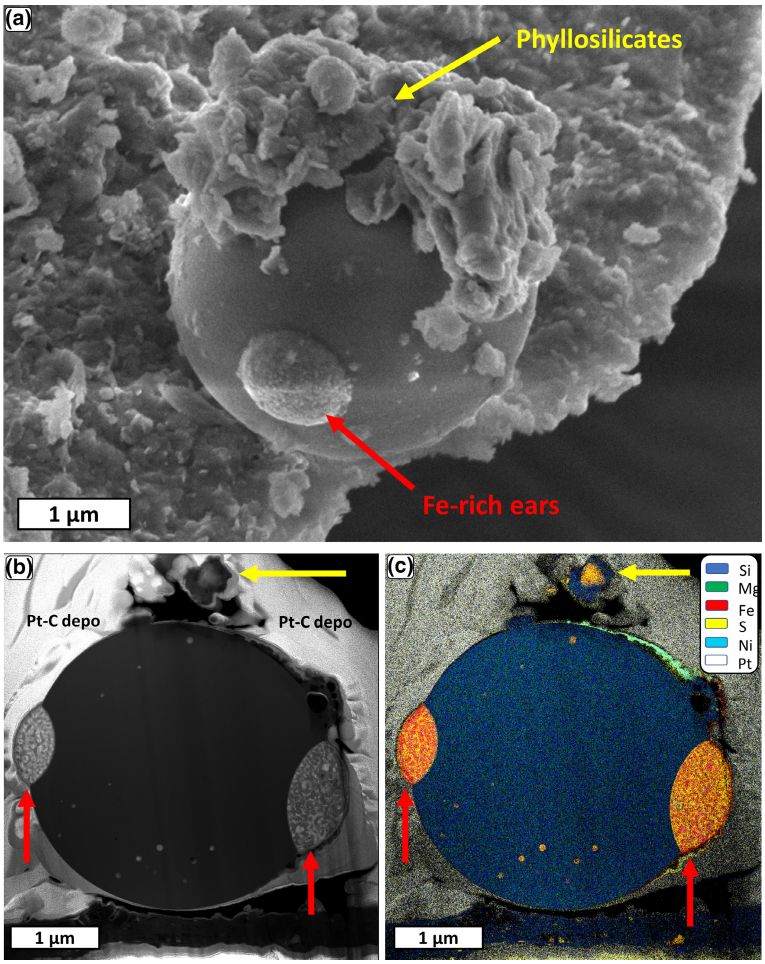

FIGURE 9. Spherical silicate droplet at the surface of grain C0105-034-017 (a) SEM image of the droplet. The droplet appears to be covered by phyllosilicates and sulfides (yellow arrow) and circular metal–sulfide areas (red arrow). (b) Cross section STEM-HAADF image of the droplet after FIB extraction. Note its perfect sphericity and the presence of two metal and sulfide lobes (red arrows). (c) The STEM-EDXS color map shows the spatial distribution of the major elements. (Color figure can be viewed at wileyonlinelibrary.com)

cooling time scales for both configurations. To do so, we will assume that the temperature reached just after the impact is 1400°C for all the following calculations.

The cooling rate of the droplet in space can be estimated using the model for silicates and glasses developed by Birnie III and Dyar (1986). This model has been specifically used in various studies to determine the cooling rate of magmatic melts in different quench media (vacuum, air, water…) (Chen et al., 2023; Hui et al., 2018; Xu & Zhang, 2002). Their model suggests that the cooling rates are mainly controlled by the sample size and the quenching medium, and that other physical property values (density, heat capacity and thermal conductivity) are less important. In order to estimate the cooling rate of the droplet, we extrapolated their 1400°C radiative model in a vacuum to a 2 µm silicate sample, resulting in an $\sim 7 \times 10^4$ K s^{-1}, implying that the equilibrium temperature of outer space (0 K) is reached within 23 ms. This high cooling rate prevents the crystallization of the silicate as it is still totally amorphous.

On the other hand, melt layers cooled mainly by conduction when the molten material encountered the asteroid surface. In order to estimate the cooling rate of this configuration, few approximations must be taken: We assume that Ryugu's surface is at ~350 K (77°C) (Shimaki et al., 2020), and that its thermal diffusivity is 3.2×10^{-7} m^2 s^{-1} (Nakamura et al., 2022). Therefore, the cooling rate of a material is given by the following Fourier's heat equation when a hot material is deposited on a cold and flat surface:

$$C_r = \alpha \cdot \frac{\Delta T}{d2}$$

where C_r is the cooling rate (K.s^{-1}), d the distance from the interface (m), ΔT the temperature difference between

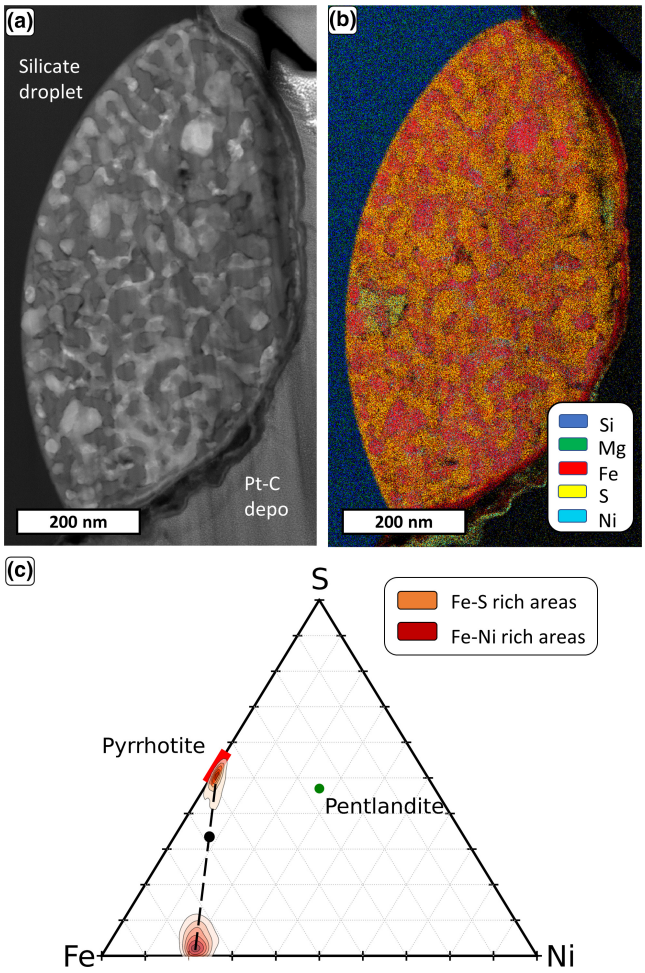

FIGURE 10. Metal–sulfide lobe at the edge of the silicate droplet. (a) STEM-HAADF image and (b) STEM-EDXS color maps of an Fe-rich lobe located at the right part of the silicate droplet surface (sample C0105-034-01701). The lobe is made of an Fe-Ni metal and Fe-sulfide mixture. Note that the outer part of the domain is covered by a thin metallic layer forming a red line on the map, right part. (c) Fe-Ni-S Ternary diagram (in atom%) of the lobe material, showing that the metallic domains are made of an Fe-Ni alloy containing 20% of Ni. The sulfide domains have a pyrrhotite composition. The average composition of this Fe-rich domain is $Fe_{0.59}Ni_{0.08}S_{0.33}$ and is represented by the black dot in the ternary diagram. (Color figure can be viewed at wileyonlinelibrary.com)

the molten silicate and the asteroid surface, and α is the thermal diffusivity. At a distance of 1 µm from the interface, that is, the typical size of a melt layer, the calculation suggests a cooling rate of $\sim 3.6 \times 10^8$ K.s^{-1}, which means that it takes approximately 3 µs for the molten material to cool from 1400 to 77°C. Within a layer of a given size, the conduction cooling rate depends on the distance to the cold interface and it explains the variation of the size distribution of sulfides within the melt layers (Figure 6). The larger cooling rate close to this interface limits the growth and coalescence and leads

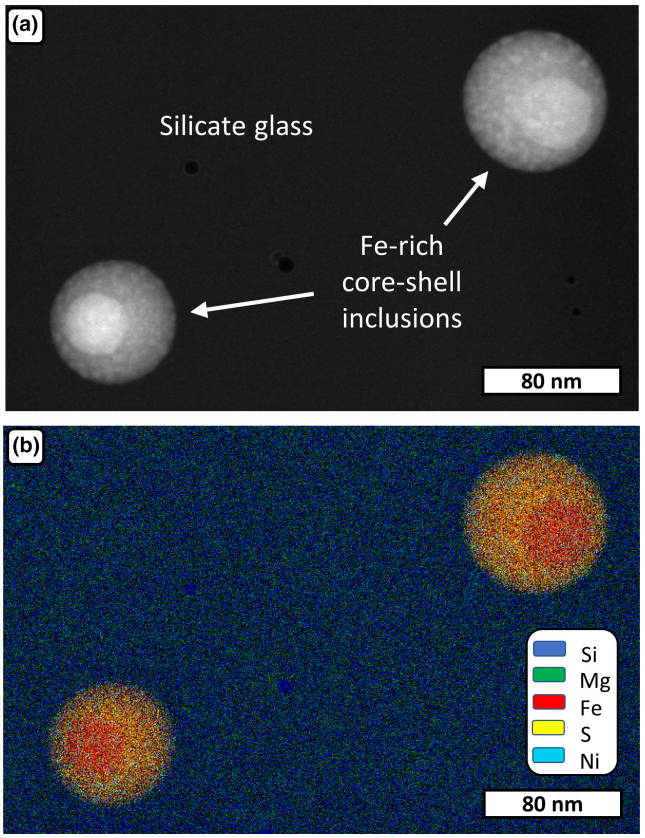

FIGURE 11. Fe-Ni-S rich inclusions trapped within the silicate droplet. (a) STEM-HAADF image and (b) STEM-EDXS color map of these inclusions. They are divided into a sulfide shell and a metallic iron core. (Color figure can be viewed at wileyonlinelibrary.com)

smaller sizes. This approach allows a comparison of the evolution of the sulfide sizes as a function of their cooling rate, that is, their distance to the interface (Figures 6 and 14). It appears that their size distribution follows a logarithmic trend with their duration of cooling, where small sulfides underwent higher cooling rates. According to the theoretical approach of Lifshitz and Slyozov (1961) concerning emulsions stabilities, the average droplet diameter varies with time as t^{α} where α scales from 1/3 to 1/2 depending on the emulsion's properties (Durian et al., 1991). This growth law describes similar trends as the logarithmic evolution of the sulfide size distributions in melt layers, confirming their rapid cooling by conduction upon encountering Ryugu's surface.

Furthermore, the occurrence of large trapped vesicles within melt layers (Figure 2) indicates that the first few nanometers of their outer surface solidified before their interior due to a rapid radiative cooling overcoming the conductive cooling. Thus, a solid thin crust is formed that prevents the vesicles from degassing.

The cooling rates presented above offer insights into the time scales involved in the different processes. During

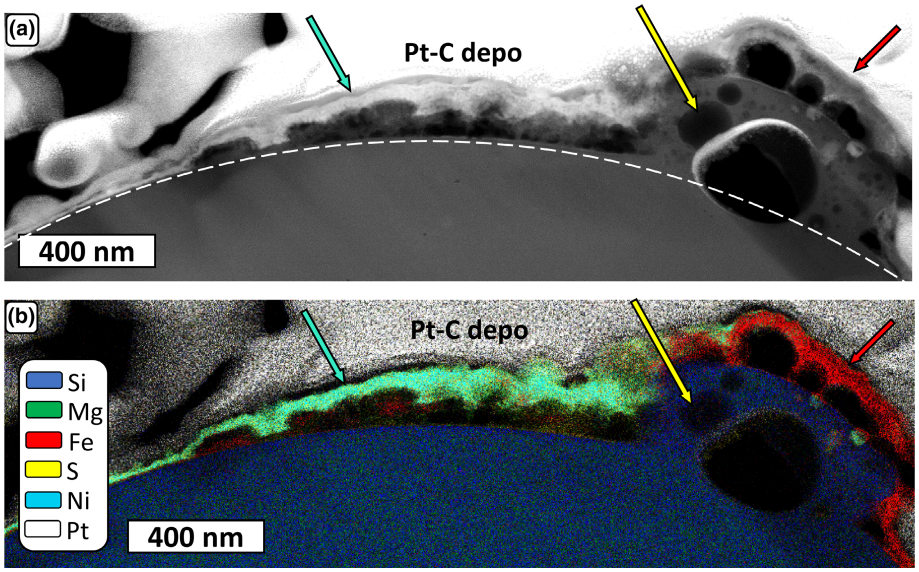

FIGURE 12. Observation of singular features at the surface of the silicate droplet, made of an Ni-S (cyan arrow), a vesiculated iron oxide (red arrow), and a vesiculated silicate layers (yellow arrow). (a) STEM-HAADF image and (b) STEM-EDXS color map of the area. The white dashed line highlights the sphericity of the droplet. STEM-EDXS spectra of the different phases are presented in Supporting Information. (Color figure can be viewed at wileyonlinelibrary.com)

TABLE 2. Comparison between the compositions (atom%) of the silicate droplet and the juxtaposed silicate vesiculated glass area on top of the droplet. Both areas were isolated by using masks based on the EDXS signal intensity of the Mg and Si elements. The mass thickness used for these quantifications was the same as in Table 1 for the silicate droplet (i.e., 5.8×10^{-2} g.cm^{-2}).

	Element												
Sample	O	Na	Mg	Al	Si	S	K	Ca	Cr	Fe	Ni	Fe/Fe + Mg	Mg + Fe/Si
C0105-034-1701 Silicate droplet	61.3	n.d.	18.2	1.6	15.7	0.1	n.d.	n.d.	0.2	2.6	n.d.	0.12	1.32
C0105-034-1701 Vesiculated silicate	62.2	2.9	15.1	1.5	14.0	0.1	0.1	0.1	0.2	3.0	0.2	0.17	1.29

the impact, the peak temperature (1400°C) is reached within a few nanoseconds, and the silicate–sulfide emulsion is formed. In the droplet that solidified before interacting with the surface, the bubbles escaped after their coalescence and migrated to the surface. A moderated to accentuated spin of the droplet might also have enhanced the coalescence and migration of the vesicles, as discussed in the case of cosmic spherules (Genge, 2017). Furthermore, their escape generates a re-equilibration of the droplet system, which induces movement of the molten sulfides in the droplet and therefore enhances their coalescence (Néri et al., 2019). For coalescence to occur, two molten sulfide droplets need to approach and drain the continuous silicate film between each other (Eggers et al., 1999; Stein, 1993; Vrij, 1966). This drainage is therefore strongly dependent on the various fluid's properties, that is, viscosity, and relative velocity of the emulsion's constituents (Bera et al., 2021). Therefore, the time required for the system to fully coalesce and equilibrate is intimately linked with the capillary forces, which describe the competition between the interfacial tensions that act as stabilizing forces and the attractive van der Waals forces that bring the droplets together and therefore act as a destabilizing force (Aarts et al., 2005; Bera et al., 2021; Eggers et al., 1999; Kralchevsky & Denkov, 2001). A potential spin of the droplet could also have enhanced the coalescence of molten sulfides and their migration to diametrically opposed sides. However, the small number of Fe-rich particles remaining in the silicate droplet and the presence of the two Fe-lobes suggest that the coalescence occurred within a millisecond or less, faster than the solidification process.

In order to estimate the surface tensions between the different phases of the droplet as well as their stabilization time, the texture and the wetting angles of these Fe-rich lobes can be used. The interface with the silicate is dominated by sulfide, whereas the interface with vacuum is dominated by metal (Figure 10a,b). In addition, the small Fe-rich inclusions in the silicate

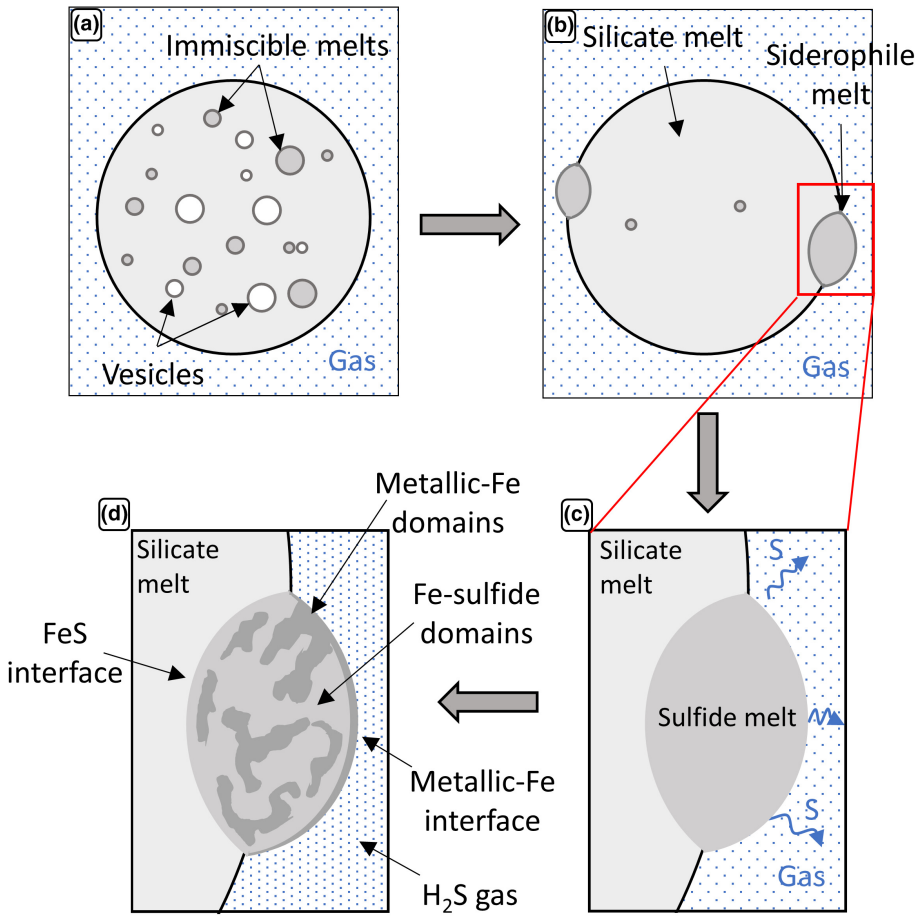

FIGURE 13. Schematic diagram describing the possible formation model for the silicate droplet after a high-temperature event. (a) Formation of a perfectly spherical melt containing two immiscible phases and vesicles. (b) The vesicles degassed and the sulfide-composition melts coalesce and migrate to the surface of the droplet, forming two diametrically opposed lobes. (c) The sulfide melts start progressively losing sulfur, leading to (d) an interconnected network of Fe-Ni metallic and Fe-sulfide domains. The droplet, as observed in this study, likely solidified at this evolution stage. (Color figure can be viewed at wileyonlinelibrary.com)

droplet have a sulfide shell and a metallic Fe-core interior (Figure 11), which confirms that the silicate-sulfide interfaces are energetically favored over silicate–metal interfaces (Holzheid et al., 2000; Matsubara et al., 2024). Silicate melts have a typical surface tension value of 0.4 $N.m^{-1}$ when exposed to vacuum (Sekiya & Nakamura, 1996). Assuming that the liquid equilibrium is reached between the different phases of the molten droplet, leads to the following surface tension values: $\gamma_{Silicate/Vacuum} = 0.4\,N\,m^{-1}$ (Sekiya & Nakamura, 1996), $\gamma_{Silicate/Fe\text{-}lobe} = 0.13\,N\,m^{-1}$, and $\gamma_{Fe\text{-}lobe/Vacuum} = 0.37\,N{\cdot}m^{-1}$ (Material S3). These surface tension values open the door to the estimation of the relaxation time of the droplet, first theorized by Tomotika (1935) and experimentally confirmed by Stone et al. (1986). By applying their model to a 1400°C silicate droplet, the stabilization time of the different phases is estimated to be less than a millisecond (Material S4).

This approach allows a rough estimate of the different time scales involved in the different processes of space weathering occurring on Ryugu's surface, summarized in Figure 15.

Scenarios for the Formation of Melt Layers

This study showed that the molten material has a composition similar to CIs and Ryugu, except for light elements (O, C, and S). It opens the door to a possible link between the melt layers and their precursors. Are melt layers made of micrometeorite impactor, or are they molten fragments of Ryugu itself? Does this molten material result from a splash? Or does it result from a local melting, without displacement of matter?

Some of the answers reside in the chemical variations that are observed. Although it is not systematic, in some cases, the silicates of the melt layer have a slightly

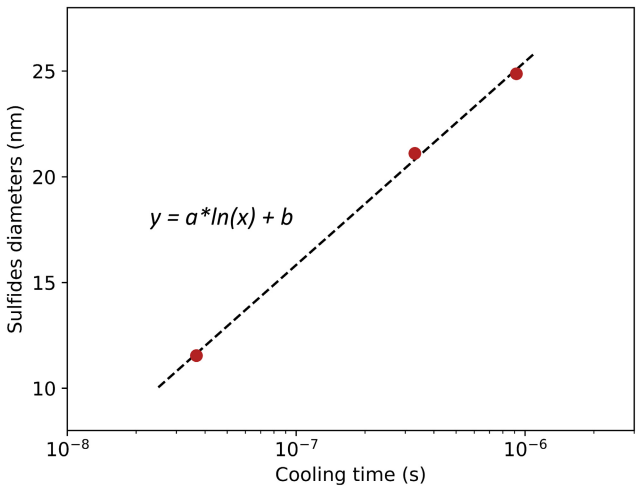

FIGURE 14. Evolution of the median sulfide diameters as a function of their time of cooling in melt layers. The cooling times of the three points were calculated using Fourier's heat equation for distances from the interface of respectively 100, 300, and 500 nm. Sulfides median diameters are taken from the statistical analysis made in Figure 6. It results in a logarithmic trend. (Color figure can be viewed at wileyonlinelibrary.com)

different Mg/Si atomic ratio compared to the underlying matrix (Figure 4b,c). These differences possibly give information about the nature of the melt layer: If the Mg/Si atomic ratios differ, it may result from a splash of another Ryugu-like lithology. If not, it might result from a local melting, without displacement of matter. However, the splashing scenario cannot be excluded.

At larger scales, it has been recognized that variations of Na concentration are present in Ryugu and indicate the presence of different lithologies (Nakamura et al., 2022). Here, the variability of the Na concentration between the melt and the underlying matrix is also remarkable. Our chemical analyses show that the bulk Na concentration fluctuates in a random manner (Table 1). This likely suggests the different lithologies of their precursors.

STEM imaging and EDXS maps are indicative of a motion of the molten material before solidification. The color map from Figure 2d shows a 250 nm thick melt layer. Its nanosulfides display elongated shapes, suggesting a movement of the molten material. It implies that this melt layer has been ejected from elsewhere as a liquid and splashed at the surface of the grain where it has been deformed before quenching. Such melt layers are also called *melt splashes* in Noguchi et al. (2023). In addition, the melt layer from Figure 1e,f shows the presence of a dense bead of rounded nanosulfides finely dispersed in the silicate. Their small size compared to the sulfides in the matrix (Figure 5) suggests that the molten material was moving to enhance the fragmentation and the dispersion of the sulfides in the silicate, forming a silicate–sulfide emulsion. Without matter displacement, such fine dispersion of sulfides would not occur. In addition, the juxtaposed matrix seems to be poor in sulfides, whereas they are omnipresent in the overlying melt layer. By extension, this melt layer might come from a different region of Ryugu, locally richer in sulfides, before splashing and quenching at the surface of the grain, forming this clear interface.

Altogether, the splashing of Ryugu-like material originating from various lithologies is likely the most common type of phenomenon that occurs after micrometeorite impacts at the surface of Ryugu.

Origin of the Silicate Droplet

The size, shape, and structure of the silicate droplet share similarities with microchondrules observed in some ordinary chondrites (Bigolski et al., 2014, 2016; Dobrică et al., 2019; Dobrică & Brearley, 2016; Krot et al., 1997) and in CM chondrites (Lee et al., 2024; Suttle, Genge, Folco, et al., 2019; Suttle, Genge, Salge, et al., 2019). These studies agree that microchondrules most likely formed after collisions between chondrules, where melt droplets escaped their parent chondrule and rapidly cooled down. In addition, vesicles and siderophile phases are also found at the edge of such microchondrules. The structural similarities imply that the formation conditions of the silicate droplet were comparable in terms of temperature, cooling processes, and overall environment.

The general composition of the silicate material of the droplet is homogeneous, but differs within the tiny vesiculated area located close to the surface (Figure 12). Whereas the droplet interior is Na depleted, this vesiculated area contains significantly more sodium (Table 2). Two hypotheses can be made: (1) Either the vesicles are remnants of the degassing process of the droplet, which did not have enough time to escape. As Na is known for its mobility in silicate melts (Mathieu et al., 2011), the Na detected in this vesiculated area might have been initially carried by the droplet, resulting in an Na-depleted droplet (Table 2). (2) Either the vesiculated area results from the impact of an external material at the surface of the droplet, which had different Na content. The presence of vesicles suggests that the molten silicate solidified before the trapped gas escaped from the melt.

Despite the relatively fast cooling of the droplet, the clear metal–sulfide segregation observed in the lobes suggests that enough time was left for the system to chemically evolve. This configuration, although the objects are smaller by several size factors, is reminiscent of the formation of sulfide-rimmed metal in chondrules from CR and CM chondrites (Singerling & Brearley, 2018). It appears that the silicate droplet studied here

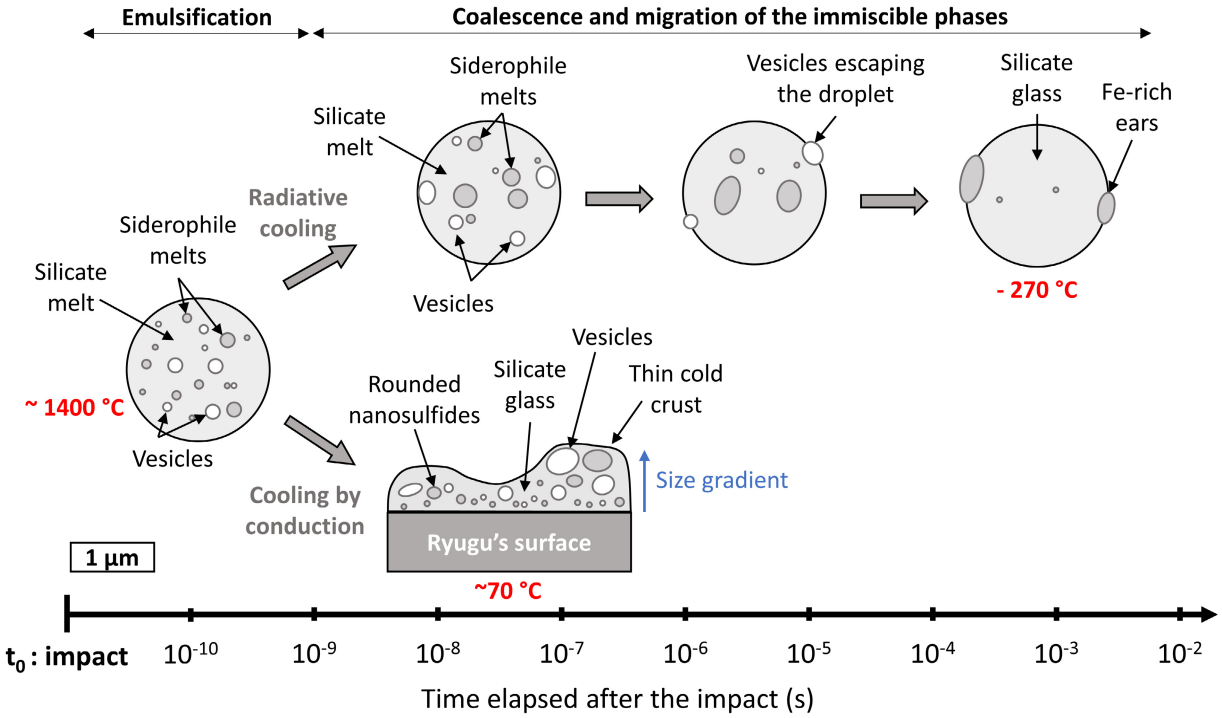

FIGURE 15. Schematic representation of the different evolution stages of the molten material depending on the cooling process undergone. Radiative cooling (upper line) produces coalescence of both the vesicles and the siderophile melts of the droplet. The vesicles escape and the Fe-rich melts migrate to the surface of the droplet in order to minimize the interfacial energies. The phase stabilization in the droplet, as well as its cooling, occurs within a millisecond after the impact. Cooling by conduction (lower line) generates a faster cooling process of the molten material and leads to the presence of rounded nanosulfides and vesicles within the melt layer. Their size varies with their distance from the interface. (Color figure can be viewed at wileyonlinelibrary.com)

displays strong similarities with one of the intermediate evolution stages of the model described by Singerling and Brearley (2018) (Figure 15). The rapid cooling of the droplet ($\sim 7 \times 10^4$ K s^{-1}) compared to millimeter-sized chondrules (10–1000 K h^{-1}, i.e., 0.003–0.3 K s^{-1}) (Hewins et al., 2005) halted the chemical evolutions that are observed in larger scale chondrules.

All in all, the origin of this singular droplet possibly results from a micrometeorite impact on Ryugu's surface. This idea is supported by the droplet volume, which is similar to those produced by impacts, that is, a few cubic micrometers. After the impact, the molten material remained suspended in space instead of splashing down on Ryugu's surface like other melt layers.

Effects on the Spectral Signature of Ryugu

The finely dispersed, rounded nanosulfides in melt layers, which are three times smaller than in the matrix (Figures 5 and 6), act as multiple scattering centers of light and therefore play a strong darkening role in the asteroid's reflectance signature, similar to what has been shown with nanophases of iron in space weathering products on the Moon and Itokawa (Hapke, 2001; Keller & McKay, 1997; Matsumoto et al., 2021; Noble et al., 2005; Noguchi et al., 2011, 2014; Sasaki et al., 2001; Thompson et al., 2014). Similar trends were also observed at the surface of comet 67P, made of silicates, sulfides, and organics (Quirico et al., 2016). Experimental approaches suggested that a fine dispersion of Fe-rich nanophases (5–40 nm) not only darkens a celestial body but also reddens it (Noble et al., 2007; Rousseau et al., 2018). A dense concentration of such phases, as observed in some melt layers of Ryugu (Figure 1e,f), is known to cause greater darkening than when dispersed in the silicate. Therefore, the presence of dense beads of nanosulfide (~20 nm in average) at the surface of Ryugu grains certainly plays a role in the extremely low albedo of the asteroid, estimated at $4.5 \pm 2\%$ at 55 µm (Sugita et al., 2019).

The structural and chemical differences between the melt layers and the underlying matrix suggest that space weathering effects may have significantly affected the Ryugu spectral signature. The oxygen loss in melt layers gives clues for the interpretation of the difference between laboratory and remote reflectance spectra. Compared to laboratory data, the NIRS3 remote sensing measurements of Ryugu's surface show a less intense

2.7 μm absorption band depth, which stands for the vibrational mode of hydroxyl groups bonded to magnesium, characteristic of phyllosilicates. By extension, this feature testifies for the initial accretion of water in the asteroid (Kitazato et al., 2019; Matsuoka et al., 2023; Pilorget et al., 2022). The dehydroxylated nature and organic depletion of the melt layers, which occur at the nanoscale, are likely to have a strong effect on the mid-infrared signature of asteroid Ryugu (Laforet et al., 2024). These modifications imply that the classifications of hydrated and carbon-rich asteroids, now based on their reflectance spectra in the mid-infrared, might be biased by the presence of these space weathering products at their surface. Indeed, if space weathering covers a large part of the surface, a carbonaceous and water-rich asteroid might appear carbon-poor and dry. At lower wavelengths, the absorption standing for the Fe^{3+} to Fe^{2+} charge transfer (0.7 μm) could also possibly be hidden by the melt layers as the Fe from melt layers is +II, whereas it is mainly +III in the underlying pristine matrix (Leroux et al., 2024; Noguchi et al., 2022).

We found that 7.5% of the 80 grains (~ 10–40 μm) observed at the University of Lille showed space weathering products on the surface of the grains, sometimes covering their entire surface (Figure 3). Only one comes from collection chamber A (*A0058_002*). The others come from chamber C, in which samples were collected below the surface of Ryugu after creating an artificial crater (Yada et al., 2022). This observation suggests that gardening effects occur on the asteroid due to successive space weathering episodes. This gardening phenomenon brings to the surface fresh and unweathered material by sputtering and burying the space weathered surface. By extension, the proportion of space weathered grains can cover a higher percentage of Ryugu's surface than estimated. Therefore, a long exposure of the asteroid surface to the harsh space environment possibly leads to a saturated surface in space weathering products. These chemical and textural processes are specific to carbonaceous and water-rich asteroids. They are likely to have a major effect on the asteroid's reflectance spectra as measured from the Earth and should be considered when classifying asteroid families.

CONCLUSION

The objective of this study was to describe quantitatively the space weathering products observed for the first time at the surface of a carbonaceous and hydrated asteroid. The structural and chemical analyses of Ryugu samples permit the interpretation of the various phenomena that led to the formation of melt layers. In particular, the high-temperature event (>1200–1300 °C), likely due to micrometeorite impacts, resulted in the loss of volatile (O, C, and S) and less volatile (Ni) elements, leading to the formation of partially to totally dehydroxylated silicates and S- and Ni-depleted sulfides. This event also led to the formation of finely dispersed, rounded nanosulfides within the melt layers, which undoubtedly contribute to the reflected light signature of the asteroid by lowering its albedo. The formation time scales for such melt layers, rapidly cooled by conduction, are estimated here to be under a microsecond. This study also identifies and characterizes a singular micrometric silicate droplet that describes an $\sim 10^4$ longer cooling process to that of melt layers. This object exhibits striking structural parallels with microchondrules and cosmic spherules.

The occurrence of space weathering products on approximately 7% of the total Hayabusa2 sample collection raises questions about the effective fraction of Ryugu's surface actually covered by such melts. The implementation of asteroid surface gardening simulations could facilitate a deeper understanding of the physical processes occurring on Ryugu's surface, thereby enabling more accurate estimations of this fraction. In total, these features may account for several percent of Ryugu's surface, resulting in significant alterations to its reflected light and, consequently, on its identification by remote sensing.

Further studies of Ryugu space weathering products, as well as Bennu's, including objects like the micrometric droplet, will assist in elucidating the diverse processes that occur at the surface of C-type asteroids.

Acknowledgments—The Hayabusa2 project has been developed and led by JAXA in collaboration with Deutsches Zentrum für Luft- und Raumfahrt (DLR) and Centre national d'études spatiales (CNES), and supported by NASA and Australian Space Agency (ASA). We thank all the members of the Hayabusa2 project for their technical and scientific contributions. This work was carried out at the electron microscopy facility of the Advanced Characterization Platform of the Chevreul Institute, University of Lille—CNRS. This project has been funded by ISITE ULNE and the "Métropole Européenne de Lille" through the "TEM-Aster project," the LARCAS ANR (Reference No. SAN-22199). The Chevreul Institute is thanked for its help in the development of this work through the CHEMACT project supported by the "Ministère de l'Enseignement Supérieur de la Recherche et de l'Innovation," the region "Hauts-de-France" and the "Métropole Européenne de Lille." The IEMN is thanked for its help for providing the FIB-SEM used for TEM sample preparation.

Data Availability Statement—Raw electron microscopy data are available for download in the Laforet

et al. (2024) Zenodo repository (https://doi.org/10.5281/zenodo.12169536).

Editorial Handling—Dr. Brearley Adrian

REFERENCES

Aarts, D. G., Lekkerkerker, H. N., Guo, H., Wegdam, G. H., and Bonn, D. 2005. Hydrodynamics of Droplet Coalescence. *Physical Review Letters* 95: 164503. https://doi.org/10.1103/PhysRevLett.95.164503.

Bera, B., Khazal, R., and Schroën, K. 2021. Coalescence Dynamics in Oil-in-Water Emulsions at Elevated Temperatures. *Scientific Reports* 11: 10990. https://doi.org/10.1038/s41598-021-89919-5.

Bigolski, J. N., Friend, A. J., Huss, G. R., Nagashima, K., and Taylor, G. J. 2016. Microchondrules in Three Unequilibrated Ordinary Chondrites. *Meteoritics & Planetary Science* 51: 235–260. https://doi.org/10.1111/maps.12585.

Bigolski, J. N., Weisberg, M. K., Ebel, D. S., and Connolly, H. C. 2014. Microchondrules: Records of Multiple Heating Events in the Solar Nebula and Implications for Type II Chondrule Formation. *45th Lunar and Planetary Science Conference*, p. 1879.

Birnie, D. P., III, and Dyar, M. D. 1986. Cooling Rate Calculations for Silicate Glasses. *Journal of Geophysical Research: Solid Earth* 91(B4): 509–513. https://doi.org/10.1029/JB091iB04p0D509.

Chapman, C. R. 2004. Space Weathering of Asteroid Surfaces. *Annual Review of Earth and Planetary Sciences* 32: 539–567. https://doi.org/10.1146/annurev.earth.32.101802.120453.

Chaves, L. C., and Thompson, M. S. 2022. Space Weathering Signatures in Sulfide and Silicate Minerals from Asteroid Itokawa. *Earth, Planets and Space* 74: 1–14. https://doi.org/10.1186/s40623-022-01683-6.

Chen, X., Zhang, Y., Hui, D., Chen, M., and Wu, Z. 2017. Study of Melting Properties of Basalt Based on their Mineral Components. *Composites Part B: Engineering* 116: 53–60. https://doi.org/10.1016/j.compositesb.2017.02.014.

Chen, Z., Zhao, Y., Chi, X., Yan, Y., Shen, J., Zou, M., Zhao, S., et al. 2023. 'Geological Timescales' Aging Effects of Lunar Glasses. *Science Advances* 9: eadi6086. https://doi.org/10.1126/sciadv.adi6086.

de la Pena, F., Ostasevicius, T., Tonaas Fauske, V., Burdet, P., Jokubauskas, P., Nord, M., Sarahan, M., et al. 2017. Electron Microscopy (Big and Small) Data Analysis with the Open Source Software Package HyperSpy. *Microscopy and Microanalysis* 23(S1): 214–15. https://doi.org/10.1017/S1431927617001751.

Dobrică, E., and Brearley, A. J. 2016. Microchondrules in Two Unequilibrated Ordinary Chondrites: Evidence for Formation by Splattering from Chondrules during Stochastic Collisions in the Solar Nebula. *Meteoritics & Planetary Science* 51: 884–905. https://doi.org/10.1111/maps.12633.

Dobrică, E., Le Guillou, C., and Brearley, A. J. 2019. Aqueous Alteration of Porous Microchondrules in Semarkona: Implications for Hydration, Oxidation and Elemental Exchange Processes. *Geochimica et Cosmochimica Acta* 244: 292–307. https://doi.org/10.1016/j.gca.2018.10.002.

Durian, D. J., Weitz, D. A., and Pine, D. J. 1991. Scaling Behavior in Shaving Cream. *Physical Review A* 44: R7902–R7905. https://doi.org/10.1103/PhysRevA.44.R7902.

Eggers, J., Lister, J. R., and Stone, H. A. 1999. Coalescence of Liquid Drops. *Journal of Fluid Mechanics* 401: 293–310. https://doi.org/10.1017/S002211209900662X.

Genge, M. J. 2017. Vesicle Dynamics during the Atmospheric Entry Heating of Cosmic Spherules. *Meteoritics & Planetary Science* 52: 443–457. https://doi.org/10.1111/maps.12805.

Genge, M. J., Alesbrook, L., Almeida, N. V., Bates, H. C., Bland, P. A., Boyd, M. R., Burchell, M. J., et al. 2023. The Fusion Crust of the Winchcombe Meteorite: A Preserved Record of Atmospheric Entry Processes. *Meteoritics & Planetary Science* 59: 948–972. https://doi.org/10.1111/maps.13937.

Genge, M. J., and Grady, M. M. 1999. The Fusion Crusts of Stony Meteorites: Implications for the Atmospheric Reprocessing of Extraterrestrial Materials. *Meteoritics & Planetary Science* 34: 341–356. https://doi.org/10.1111/j.1945-5100.1999.tb01344.x.

Gu, L., Chen, Y., Xu, Y., Tang, X., Lin, Y., Noguchi, T., and Li, J. 2022. Space Weathering of the Chang'e-5 Lunar Sample from a Mid-High Latitude Region on the Moon. *Geophysical Research Letters* 49: e2022GL097875. https://doi.org/10.1029/2022GL097875.

Guo, J.-G., Ying, T., Gao, H., Chen, X., Song, Y., Lin, T., Zhang, Q., et al. 2022. Surface Microstructures of Lunar Soil Returned by Chang'e-5 Mission Reveal an Intermediate Stage in Space Weathering Process. *Science Bulletin* 67: 1696–1701. https://doi.org/10.1016/j.scib.2022.06.019.

Hapke, B. 2001. Space Weathering from Mercury to the Asteroid Belt. *Journal of Geophysical Research: Planets* 106(E5): 10039–73. https://doi.org/10.1029/2000JE001338.

Hewins, R. H., Connolly, H. C., Lofgren, G. E., and Libourel, G. 2005. Experimental Constraints on Chondrule Formation. In *Chondrites and the Protoplanetary Disk*, vol. 341, 286. San Francisco, Astronomical Society of the Pacific.

Holzheid, A., Schmitz, M. D., and Grove, T. L. 2000. Textural Equilibria of Iron Sulfide Liquids in Partly Molten Silicate Aggregates and their Relevance to Core Formation Scenarios. *Journal of Geophysical Research: Solid Earth* 105(B6): 13555–67. https://doi.org/10.1029/2000JB900046.

Hsieh, K.-C., Chang, Y. A., and Zhong, T. 1982. The Fe- Ni- S System above 700°C (Iron- Nickel- Sulfur). *Bulletin of Alloy Phase Diagrams* 3: 165–172. https://doi.org/10.1007/BF02892375.

Huang, T., Huang, T.-. J., Ganju, E., Torbatisarraf, H., Thompson, M. S., and Chawla, N. 2024. Advanced Microstructural and Compositional Analysis of a Lunar Agglutinate from the Apollo 11 Mission. *Meteoritics & Planetary Science* 59: 14157. https://doi.org/10.1111/maps.14157.

Hui, H., Hess, K. U., Zhang, Y., Nichols, A. R. L., Peslier, A. H., Lange, R. A., Dingwell, D. B., and Neal, C. R. 2018. Cooling Rates of Lunar Orange Glass Beads. *Earth and Planetary Science Letters* 503: 88–94. https://doi.org/10.1016/j.epsl.2018.09.019.

Ito, M., et al. 2022. A Pristine Record of Outer Solar System Materials from Asteroid Ryugu's Returned Sample.

Nature Astronomy 6: 1163–71. https://doi.org/10.1038/s41550-022-01745-5.
Keller, L. P., and McKay, D. S. 1997. The Nature and Origin of Rims on Lunar Soil Grains. *Geochimica et Cosmochimica Acta* 61: 2331–41. https://doi.org/10.1016/S0016-7037(97)00085-9.
King, A. J., et al. 2022. The Winchcombe Meteorite, a Unique and Pristine Witness from the Outer Solar System. *Science Advances* 8: eabq3925. https://doi.org/10.1126/sciadv.abq3925.
Kitazato, K., Milliken, R. E., Iwata, T., Abe, M., Ohtake, M., Matsuura, S., Arai, T., et al. 2019. The Surface Composition of Asteroid 162173 Ryugu from Hayabusa2 near-Infrared Spectroscopy. *Science* 364: 272–75. https://doi.org/10.1126/science.aav7432.
Kitazato, K., Milliken, R. E., Iwata, T., Abe, M., Ohtake, M., Matsuura, S., Takagi, Y., et al. 2021. Thermally Altered Subsurface Material of Asteroid (162173) Ryugu. *Nature Astronomy* 5: 246–250. https://doi.org/10.1038/s41550-020-01271-2.
Kralchevsky, P. A., and Denkov, N. D. 2001. Capillary Forces and Structuring in Layers of Colloid Particles. *Current Opinion in Colloid & Interface Science* 6: 383–401. https://doi.org/10.1016/S1359-0294(01)00105-4.
Krot, A. N., Rubin, A. E., Keil, K., and Wasso, J. T. 1997. Microchondrules in Ordinary Chondrites: Implications for Chondrule Formation. *Geochimica et Cosmochimica Acta* 61: 463–473. https://doi.org/10.1016/S0016-7037(96)00342-0.
Laforet, S., Le Guillou, C., de la Peña, F., Walls, M., Tizei, L. H. G., Marinova, M., Beck, P., et al. 2024. Linking Cause and Effect: Nanoscale Vibrational Spectroscopy of Space Weathering from Asteroid Ryugu. *The Astrophysical Journal Letters* 963: L45. https://doi.org/10.3847/2041-8213/ad2b65.
Lee, M. R., Daly, L., Greer, J., Griffin, S., Floyd, C. J., Tegg, L., and Cairney, J. 2024. Shock Melt in the Cold Bokkeveld CM2 Carbonaceous Chondrite and the Response of C-Complex Asteroids to Hypervelocity Impacts. *Meteoritics & Planetary Science* 59: 2818–30. https://doi.org/10.1111/maps.14253.
Leroux, H. 2012. Fine-Grained Material of 81P/Wild 2 in Interaction with the Stardust Aerogel. *Meteoritics & Planetary Science* 47: 613–622. https://doi.org/10.1111/j.1945-5100.2011.01309.x.
Leroux, H., Le Guillou, C., Marinova, M., Laforet, S., Viennet, J.-. C., Mouloud, B.-. E., Teurtrie, A., et al. 2024. Phyllosilicates with Embedded Fe-Based Nanophases in Ryugu and Orgueil. *Meteoritics & Planetary Science* 59: 1947–65. https://doi.org/10.1111/maps.14101.
Leroux, H., Rietmeijer, F. J. M., Velbel, M. A., Brearley, A. J., Jacob, D., Langenhorst, F., Bridges, J. C., et al. 2008. A TEM Study of Thermally Modified Comet 81P/Wild 2 Dust Particles by Interactions with the Aerogel Matrix during the Stardust Capture Process. *Meteoritics & Planetary Science* 43: 97–120. https://doi.org/10.1111/j.1945-5100.2008.tb00612.x.
Lifshitz, I. M., and Slyozov, V. V. 1961. The Kinetics of Precipitation from Supersaturated Solid Solutions. *Journal of Physics and Chemistry of Solids* 19: 35–50. https://doi.org/10.1016/0022-3697(61)90054-3.
Loeffler, M. J., Dukes, C. A., Chang, W. Y., McFadden, L. A., and Baragiola, R. A. 2008. Laboratory Simulations of Sulfur Depletion at Eros. *Icarus* 195: 622–29. https://doi.org/10.1016/j.icarus.2008.02.002.
Love, S. G., and Brownlee, D. E. 1991. Heating and Thermal Transformation of Micrometeoroids Entering the Earth's Atmosphere. *Icarus* 89: 26–43. https://doi.org/10.1016/0019-1035(91)90085-8.
Mathieu, R., Libourel, G., Deloule, E., Tissandier, L., Rapin, C., and Podor, R. 2011. Na_2O Solubility in CaO–MgO–SiO_2 Melts. *Geochimica et Cosmochimica Acta* 75: 608–628. https://doi.org/10.1016/j.gca.2010.11.001.
Matsubara, S., Terasaki, H., Yoshino, T., Urakawa, S., and Yumitori, D. 2024. Wetting Property of Fe-S Melt in Solid Core: Implication for the Core Crystallization Process in Planetesimals. *Meteoritics & Planetary Science* 59: 1314–28 Available at: 10.1111/maps.14149.
Matsumoto, M., Matsuno, J., Tsuchiyama, A., Nakamura, T., Enokido, Y., Kikuiri, M., Nakato, A., et al. 2024. Microstructural and Chemical Features of Impact Melts on Ryugu Particle Surfaces: Records of Interplanetary Dust Hit on Asteroid Ryugu. *Science Advances* 10: eadi7203. https://doi.org/10.1126/sciadv.adi7203.
Matsumoto, T., Harries, D., Langenhorst, F., Miyake, A., and Noguchi, T. 2020. Iron Whiskers on Asteroid Itokawa Indicate Sulfide Destruction by Space Weathering. *Nature Communications* 11: 1117. https://doi.org/10.1038/s41467-020-14758-3.
Matsumoto, T., Noguchi, T., Tobimatsu, Y., Harries, D., Langenhorst, F., Miyake, A., and Hidaka, H. 2021. Space Weathering of Iron Sulfides in the Lunar Surface Environment. *Geochimica et Cosmochimica Acta* 299: 69–84. https://doi.org/10.1016/j.gca.2021.02.013.
Matsumoto, T., Noguchi, T., Miyake, A., Igami, Y., Haruta, M., Seto, Y., Miyahara, M., et al. 2023. Influx of Nitrogen-Rich Material from the Outer Solar System Indicated by Iron Nitride in Ryugu Samples. *Nature Astronomy* 8(2): 207–215.
Matsumoto, T., Noguchi, T., Miyake, A., Igami, Y., Haruta, M., Saito, H., Hata, S., et al. 2022. Space Weathering of Anhydrous Minerals in Regolith Samples from the c-Type Asteroid Ryugu. *53rd Lunar and Planetary Science Conference*, p. 1693.
Matsuoka, M., Kagawa, E., Amano, K., Nakamura, T., Tatsumi, E., Osawa, T., Hiroi, T., et al. 2023. Space Weathering Acts Strongly on the Uppermost Surface of Ryugu. *Communications Earth & Environment* 4: 335 Available at: 10.1038/s43247-023-00991-3.
Michel, P., Ballouz, R. L., Barnouin, O. S., Jutzi, M., Walsh, K. J., May, B. H., Manzoni, C., et al. 2020. Collisional Formation of Top-Shaped Asteroids and Implications for the Origins of Ryugu and Bennu. *Nature Communications* 11: 2655. https://doi.org/10.1038/s41467-020-16433-z.
Nakamura, T., Matsumoto, M., Amano, K., Enokido, Y., Zolensky, M. E., Mikouchi, T., Genda, H., et al. 2022. Formation and Evolution of Carbonaceous Asteroid Ryugu: Direct Evidence from Returned Samples. *Science* 379: 6634. eabn8671.
Nakato, A., Yada, T., Nishimura, M., Yogata, K., Miyazaki, A., Nagashima, K., Hatakeda, K., et al. 2023. Variations of the Surface Characteristics of Ryugu Returned Samples. *Earth, Planets and Space* 75: 45. https://doi.org/10.1186/s40623-022-01754-8.
Néri, A., Guignard, J., Monnereau, M., Toplis, M. J., and Quitté, G. 2019. Metal Segregation in Planetesimals: Constraints from Experimentally Determined Interfacial Energies. *Earth and Planetary Science Letters* 518: 40–52. https://doi.org/10.1016/j.epsl.2019.04.049.

Noble, S. K., Keller, L. P., and Pieters, C. M. 2005. Evidence of Space Weathering in Regolith Breccias I: Lunar Regolith Breccias. *Meteoritics & Planetary Science* 40: 397–408.

Noble, S. K., Pieters, C. M., and Keller, L. P. 2007. An Experimental Approach to Understanding the Optical Effects of Space Weathering. *Icarus* 192: 629–642. https://doi.org/10.1016/j.icarus.2007.07.021.

Noguchi, T., Kimura, M., Hashimoto, T., Konno, M., Nakamura, T., Zolensky, M. E., Okazaki, R., et al. 2014. Space Weathered Rims Found on the Surfaces of the Itokawa Dust Particles. *Meteoritics & Planetary Science* 49: 188–214. https://doi.org/10.1111/maps.12111.

Noguchi, T., Matsumoto, T., Miyake, A., Igami, Y., Haruta, M., Saito, H., Hata, S., et al. 2023. Mineralogy and Petrology of Fine-Grained Samples Recovered from the Asteroid (162173) Ryugu. *Meteoritics & Planetary Science* 59: 1877–1906. https://doi.org/10.1111/maps.14093.

Noguchi, T., Matsumoto, T., Miyake, A., Igami, Y., Haruta, M., Saito, H., Hata, S., et al. 2022. A Dehydrated Space-Weathered Skin Cloaking the Hydrated Interior of Ryugu. *Nature Astronomy* 7: 170–181.

Noguchi, T., Nakamura, T., Kimura, M., Zolensky, M. E., Tanaka, M., Hashimoto, T., Konno, M., et al. 2011. Incipient Space Weathering Observed on the Surface of Itokawa Dust Particles. *Science* 333: 1121–25. https://doi.org/10.1126/science.1207794.

Noguchi, T., Nakamura, T., Okudaira, K., Yano, H., Sugita, S., and Burchell, M. J. 2007. Thermal Alteration of Hydrated Minerals during Hypervelocity Capture to Silica Aerogel at the Flyby Speed of Stardust. *Meteoritics & Planetary Science* 42: 357–372 Available at: 10.1111/j.1945-5100.2007.tb00239.x.

Nozaki, W., Nakamura, T., and Noguchi, T. 2006. Bulk Mineralogical Changes of Hydrous Micrometeorites during Heating in the Upper Atmosphere at Temperatures below 1000 °C. *Meteoritics & Planetary Science* 41: 1095–1114. https://doi.org/10.1111/j.1945-5100.2006.tb00507.x.

Okazaki, R., Marty, B., Busemann, H., Hashizume, K., Gilmour, J. D., Meshik, A., Yada, T., et al. 2023. Noble Gases and Nitrogen in Samples of Asteroid Ryugu Record its Volatile Sources and Recent Surface Evolution. *Science* 379: eabo0431. https://doi.org/10.1126/science.abo0431.

Panerai, F., Bessire, B., Haskins, J., Foster, C., Barnard, H., Stern, E., and Feldman, J. 2021. Morphological Evolution of Ordinary Chondrite Microstructure during Heating: Implications for Atmospheric Entry. *The Planetary Science Journal* 2: 179. https://doi.org/10.3847/PSJ/ac1749.

Pieters, C. M., and Noble, S. K. 2016. Space Weathering on Airless Bodies. *Journal of Geophysical Research: Planets* 121: 1865–84. https://doi.org/10.1002/2016JE005128.

Pilorget, C., et al. 2022. First Compositional Analysis of Ryugu Samples by the MicrOmega Hyperspectral Microscope. *Nature Astronomy* 6: 221–25. https://doi.org/10.1038/s41550-021-01549-z.

Quirico, E., Moroz, L. V., Schmitt, B., Arnold, G., Faure, M., Beck, P., Bonal, L., et al. 2016. Refractory and Semi-Volatile Organics at the Surface of Comet 67P/Churyumov-Gerasimenko: Insights from the VIRTIS/Rosetta Imaging Spectrometer. *Icarus* 272: 32–47. https://doi.org/10.1016/j.icarus.2016.02.028.

Rousseau, B., Érard, S., Beck, P., Quirico, É., Schmitt, B., Brissaud, O., Montes-Hernandez, G., et al. 2018. Laboratory Simulations of the vis-NIR Spectra of Comet 67P Using Sub-µm Sized Cosmochemical Analogues. *Icarus* 306: 306–318. https://doi.org/10.1016/j.icarus.2017.10.015.

Sasaki, S., Nakamura, K., Hamabe, Y., Kurahashi, E., and Hiroi, T. 2001. Production of Iron Nanoparticles by Laser Irradiation in a Simulation of Lunar-like Space Weathering. *Nature* 410: 555–57. https://doi.org/10.1038/35069013.

Schindelin, J., Arganda-Carreras, I., Frise, E., Kaynig, V., Longair, M., Pietzsch, T., Preibisch, S., et al. 2012. Fiji: An Open-Source Platform for Biological-Image Analysis. *Nature Methods* 9: 676–682. https://doi.org/10.1038/nmeth.2019.

Schneider, C. A., Rasband, W. S., and Eliceiri, K. W. 2012. NIH Image to ImageJ: 25 Years of Image Analysis. *Nature Methods* 9: 671–75. https://doi.org/10.1038/nmeth.2089.

Sekiya, M., and Nakamura, T. 1996. Condition for the Formation of the Compound Chondrules in the Solar Nebula Twentieth Symposium on Antarctic Meteorites. Proceedings of the NIPR Symposium, No. 9, held June 6-8, 1995, at the National Institute of Polar Research, Tokyo. Editor in Chief, Hideyasu Kojima, with Naoya Imae, Makoto Kimura, Akira Shimoyama, Nobuo Takaoka. Published by the National Institute of Polar Research, p. 208.

Shaw, H. R. 1969. Rheology of Basalt in the Melting Range. *Journal of Petrology* 10: 510–535. https://doi.org/10.1093/petrology/10.3.510.

Shimaki, Y., Senshu, H., Sakatani, N., Okada, T., Fukuhara, T., Tanaka, S., Taguchi, M., et al. 2020. Thermophysical Properties of the Surface of Asteroid 162173 Ryugu: Infrared Observations and Thermal Inertia Mapping. *Icarus* 348: 113835. https://doi.org/10.1016/j.icarus.2020.113835.

Singerling, S. A., and Brearley, A. J. 2018. Primary Iron Sulfides in CM and CR Carbonaceous Chondrites: Insights into Nebular Processes. *Meteoritics & Planetary Science* 53: 2078–2106. https://doi.org/10.1111/maps.13108.

Stein, H. N. 1993. The Drainage of Free Liquid Films. *Colloids and Surfaces A: Physicochemical and Engineering Aspects* 79: 71–80. https://doi.org/10.1016/0927-7757(93)80161-7.

Stone, H. A., Bentley, B. J., and Leal, L. G. 1986. An Experimental Study of Transient Effects in the Breakup of Viscous Drops. *Journal of Fluid Mechanics* 173: 131–158. https://doi.org/10.1017/S0022112086001118.

Sugita, S., Honda, R., Morota, T., Kameda, S., Sawada, H., Tatsumi, E., Yamada, M., et al. 2019. The Geomorphology, Color, and Thermal Properties of Ryugu: Implications for Parent-Body Processes. *Science* 364: eaaw0422. https://doi.org/10.1126/science.aaw0422.

Suttle, M. D., Daly, L., Jones, R. H., Jenkins, L., van Ginneken, M., Mitchell, J. T., Bridges, J. C., et al. 2022. The Winchcombe Meteorite—A Regolith Breccia from a Rubble Pile CM Chondrite Asteroid. *Meteoritics & Planetary Science* 59: 1043–67. https://doi.org/10.1111/maps.13938.

Suttle, M. D., Genge, M. J., Folco, L., Van Ginneken, M., Lin, Q., Russell, S. S., and Najorka, J. 2019. The Atmospheric Entry of Fine-Grained Micrometeorites: The Role of Volatile Gases in Heating and Fragmentation. *Meteoritics & Planetary Science* 54: 503–520. https://doi.org/10.1111/maps.13220.

Suttle, M. D., Genge, M. J., Salge, T., Lee, M. R., Folco, L., Góral, T., Russell, S. S., and Lindgren, P. 2019. A Microchondrule-Bearing Micrometeorite and Comparison

with Microchondrules in CM Chondrites. *Meteoritics & Planetary Science* 54: 1303–24. https://doi.org/10.1111/maps.13279.

Taylor, S., Jones, K. W., Herzog, G. F., and Hornig, C. E. 2011. Tomography: A Window on the Role of Sulfur in the Structure of Micrometeorites. *Meteoritics & Planetary Science* 46: 1498–1509.

Thompson, M. S., Christoffersen, R., Zega, T. J., and Keller, L. P. 2014. Microchemical and Structural Evidence for Space Weathering in Soils from Asteroid Itokawa. *Earth, Planets and Space* 66: 1–10. https://doi.org/10.1186/1880-5981-66-89.

Tomotika, S. 1935. On the Instability of a Cylindrical Thread of a Viscous Liquid Surrounded by another Viscous Fluid. *Proceedings of the Royal Society of London. Series A: Mathematical and Physical Sciences* 150: 322–337.

Vrij, A. 1966. Possible Mechanism for the Spontaneous Rupture of Thin, Free Liquid Films. *Discussions of the Faraday Society* 42: 23–33. https://doi.org/10.1039/df9664200023.

Waldner, P., and Pelton, A. D. 2004. Critical Thermodynamic Assessment and Modeling of the Fe-Ni-S System. *Metallurgical and Materials Transactions B* 35: 897–907. https://doi.org/10.1007/s11663-004-0084-7.

Watanabe, S., et al. 2019. Hayabusa2 Arrives at the Carbonaceous Asteroid 162173 Ryugu—A Spinning Top–Shaped Rubble Pile. *Science* 364: 268–272. https://doi.org/10.1126/science.aav8032.

Xu, Z., and Zhang, Y. 2002. Quench Rates in Air, Water, and Liquid Nitrogen, and Inference of Temperature in Volcanic Eruption Columns. *Earth and Planetary Science Letters* 200: 315–330. https://doi.org/10.1016/S0012-821X(02)00656-8.

Yabuta, H., Cody, G. D., Engrand, C., Kebukawa, Y., De Gregorio, B., Bonal, L., Remusat, L., et al. 2023. Macromolecular Organic Matter in Samples of the Asteroid (162173) Ryugu. *Science* 379: eabn9057. https://doi.org/10.1126/science.abn9057.

Yada, T., Abe, M., Okada, T., Nakato, A., Yogata, K., Miyazaki, A., Hatakeda, K., et al. 2022. Preliminary Analysis of the Hayabusa2 Samples Returned from C-Type Asteroid Ryugu. *Nature Astronomy* 6: 214–220. https://doi.org/10.1038/s41550-021-01550-6.

Yokoyama, T., Nagashima, K., Nakai, I., Young, E. D., Abe, Y., Aléon, J., Alexander, C. M. O., et al. 2022. Samples Returned from the Asteroid Ryugu Are Similar to Ivuna-Type Carbonaceous Meteorites. *Science 379: 6634*: eabn7850.

SUPPORTING INFORMATION

Additional supporting information may be found in the online version of this article.

Figure S0. Complementary SEM images of Ryugu grains.

Figure S1. STEM-EDXS Principal Component Analysis on the Fe-S-rich inclusions of the silicate droplet.

Figure S2. STEM-EDXS mean spectra of the different phases present in Fig. 11.

Figure S3. Determination of surface tensions in the equilibrated droplet.

Data S4. Determination of the relaxation time of the silicate droplet.